Supporting Information for: 'SLAMS-2.0: a Stochastic, Lagrangian Aggregate Model of Sinking Particles for the Ocean's Biological Carbon Pump, version 2'

A. Rufas[1], S. Khatiwala[2], T. Jokulsdottir

[1]Department of Earth Sciences, University of Oxford, Oxford, UK

[2]School of International Liberal Studies, Waseda University, Tokyo, Japan

Contents of this file

Texts S1–S3 detail the datasets used in this study, including prescribed fields, related input variables, and observational constraints to assess model performance. **Texts S4–S5** detail the governing equations for particle state and mesozooplankton characteristics.

Figures S1–S6 illustrate the prescribed datasets and observational constraints, including a validation of prescribed NPP. **Figure S7** compares particle size distributions and mass concentrations produced by the sectional method and the SLAMS-2.0 coagulation scheme, while **Figures S8–S9** show the sensitivity of export POC flux and particle number concentration to one-at-a-time parameter perturbations.

Table S1 provides quantitative validation of prescribed NPP, and **Table S2** lists depth ranges for the key horizons used in model-data comparisons.

Corresponding author: A. Rufas (Anna.RufasBlanco@earth.ox.ac.uk)

Text S1. Observational Datasets for Model Forcing

For the simulations presented here, the following datasets are used (**Figure S1**).

- Surface ocean photosynthetically active radiation (PAR_0, $\mathrm{W\,m^{-2}}$) is derived from monthly climatologies of Aqua-MODIS Level 3 satellite data, available via NASA's Ocean Color portal (`https://oceancolor.gsfc.nasa.gov/l3/order/`).

- Aeolian dust deposition flux ($\mathrm{g\,clay\,m^{-2}\,s^{-1}}$) was sourced from the historical run (1850–2014) of the NCAR-CESM2 model, part of the Coupled Model Intercomparison Project Phase 6 (CMIP6). The dataset has monthly and 100 km spatial resolution and was obtained via the Earth System Grid Federation (`https://esgf-node.llnl.gov/projects/cmip6/`). Dust fluxes were converted to clay fluxes using a 0.5:1 clay-to-dust mass ratio, following Journet, Desboeufs, Caquineau, and Colin (2008, Table 1).

- Net primary production integrated over the euphotic zone (NPP, $\mathrm{mg\,C\,m^{-2}\,d^{-1}}$) is obtained from the ESA BICEP v4.2 multi-sensor monthly climatology (Kulk et al., 2021). NPP is distributed over the daylight fraction of the modelled day and converted to $\mathrm{mol\,C\,m^{-2}\,s^{-1}}$ for the time steps receiving PAR_0. Among several satellite-based NPP products (**Figure S2**), BICEP was selected to force SLAMS-2.0 due to its closer agreement with available *in situ* ^{14}C uptake measurements at our study sites (**Figure S3** and **Table S1**).

- Chlorophyll *a* concentration integrated over the euphotic layer (Chl*a*, $\mathrm{mg\,m^{-3}}$) is obtained from the multi-sensor monthly climatology of ESA's Ocean Colour Climate Change Initiative (OC-CCI) v6 and available at the OC-CCI website (`https://www.oceancolour.org`), after Sathyendranath et al. (2023).

- Mixed layer depth (MLD, m) is from the monthly climatology of De Boyer Montégut, Madec, Fischer, Lazar, and Iudicone (2004) that applies a variable density threshold equivalent to a 0.2°C temperature decrease. The dataset is available from the IFREMER/LOPS Mixed Layer Depth Climatology portal (`http://www.ifremer.fr/cerweb/deboyer/mld/`).

- Seawater temperature (°C), salinity (PSU), dissolved O_2 concentration ($\mathrm{mL\,L^{-1}}$), and macronutrient concentration (nitrate, phosphate, and silicate; $\mathrm{mmol\,m^{-3}}$) are from World Ocean Atlas 2023 (WOA23) monthly climatologies (`https://www.ncei.noaa.gov/access/world-ocean-atlas-2023/`, Reagan et al., 2024). Since WOA23 monthly fields are depth-limited (e.g., temperature and O_2 to 1500 m; nutrients to 800 m), deeper layers were filled using corresponding annual climatologies to produce full-depth profiles.

- Seawater density (ρ_{w}, $\mathrm{g\,cm^{-3}}$) and dynamic viscosity (μ, $\mathrm{g\,cm^{-1}\,s^{-1}}$) were calculated from WOA23 temperature and salinity fields. Density was computed using the Gibbs-SeaWater (GSW) Oceanographic Toolbox (MATLAB, v3.06, `https://www.teos-10.org/`) based on the Thermodynamic Equations of Seawater–2010 (TEOS-10) McDougall and Barker (2011). Dynamic viscosity was derived using routines from the MIT seawater properties library (MATLAB, v3.1.5, `https://web.mit.edu/seawater/`) following the formulations of Sharqawy, Lienhard, and Zubair (2010) and Nayar, Sharqawy, Banchik, and Lienhard (2016).

- Calcite saturation state is calculated using CO2SYS (MATLAB, v.1.1, Lewis & Wallace, 1998; Van Heuven et al., 2011), with default dissociation constants and incorporating annual climatological data of alkalinity, CO_2, temperature, salinity, silicate, and phosphate from the Global Ocean Data Analysis Project version 2 (GLODAPv2.2016b, `https://`

`www.nodc.noaa.gov/archive/arc0107/0162565/2.2/data/0-data/mapped/`, Olsen et al., 2016).

- Lastly, mesozooplankton biomass ($\mathrm{mg\,C\,m^{-3}}$) is obtained from the CMIP6 Earth System Model IPSL-CM6A-LR, developed by the Institut Pierre Simon Laplace (IPSL), France. Data were downloaded from the Earth System Grid Federation (ESGF) Lawrence Livermore National Laboratory node (`http://esgf-node.llnl.gov/search/cmip6/?mip_era=CMIP6&activity_id=CMIP&institution_id=IPSL&source_id=IPSL-CM6A-LR/`). IPSL-CM6A-LR uses the biogeochemical ecosystem model PISCES-v2.0 (Aumont et al., 2015), which resolves the full water column. We use the monthly climatology from the historical IPSL-CM6A-LR simulation (1997–2014; r1i1p1f1). PISCES-v2.0 was selected because it shows strong agreement with observational mesozooplankton biomass when evaluated against MAREDAT using a Generalized Linear Mixed Model approach (Petrik et al., 2022; Moriarty & O'Brien, 2013). We note that CMIP6 models define mesozooplankton as organisms in the 20–200 µm size range (definitions here: `https://clipc-services.ceda.ac.uk/dreq/mipVars.html`), whereas whereas the MAREDAT classification uses a 200–2000 µm definition (Sieburth et al., 1978).

Text S2. Derived Physical and Optical Fields

The prescribed forcing fields described in **Text S1** are used to calculate the physical and light-related quantities described below.

Water Physics

In SLAMS-2.0, water physics is parameterised through two foundational variables —dynamic viscosity and turbulent kinetic energy (TKE) dissipation rate— from which additional hydrodynamic quantities are derived.

Prescribed dynamic viscosity, μ ($\mathrm{g\,cm^{-1}\,s^{-1}}$), is used to derive the kinematic viscosity, ν ($\mathrm{cm^2\,s^{-1}}$), as

$$\nu = \frac{\mu}{\rho_\mathrm{w}}. \tag{1}$$

The TKE dissipation rate, ϵ ($\mathrm{m^2\,s^{-3}}$), characterises the rate at which energy from wind- and tide-driven stirring cascades to small scales and is dissipated through molecular viscosity, generating turbulent mixing. In SLAMS-2.0, ϵ is sampled via Monte Carlo from a log-normal distribution, as form commonly assumed in global ocean models (Pearson & Fox-Kemper, 2018):

$$f(\epsilon) = \frac{1}{\epsilon \cdot \sigma \cdot \sqrt{2\pi}} \cdot e^{-\left(\dfrac{(\ln \epsilon - \mu)^2}{2\sigma^2}\right)}, \tag{2}$$

with typical values of $\log_{10}(\epsilon) \in [-7, -4]$ $\mathrm{m^2\,s^{-3}}$ for shelf seas and coastal waters (depth < 200 m), and $[-9, -6]$ $\mathrm{m^2\,s^{-3}}$ for the open ocean (Saiz & Kiørboe, 1995). Here, μ is the logarithmic mean, $\mu = \ln[\sum(\epsilon)/n]$, and σ the variance of the distribution, set to 1.2. Although ϵ varies spatially and with depth (Pearson & Fox-Kemper, 2018), SLAMS-2.0 assumes a vertically uniform distribution since variations with depth are small.

From ν and ϵ, two additional hydrodynamic quantities are derived: the water shear rate, γ (s^{-1}), which quantifies velocity gradients caused by turbulent mixing:

$$\gamma = \left(\frac{\epsilon}{\nu}\right)^{1/2}, \tag{3}$$

and the Kolmogorov length scale, η (m), which represents the smallest turbulent eddy size below which fluid viscosity dominates and all turbulent kinetic energy is dissipated (as heat) instead of creating turbulent motion,

$$\eta = \left(\frac{\nu^3}{\epsilon}\right)^{1/4}. \tag{4}$$

Water Light-Related Fields

SLAMS-2.0 requires the calculation of three light-related fields: (i) photoperiod, (ii) vertical attenuation of PAR, and (iii) euphotic zone depth. Together, these fields control the timing and depth of phytoplankton growth and zooplankton vertical migration.

The photoperiod, or number of daylight hours at the ocean surface, $n_{\mathrm{h}}(\phi, t)$, depends on latitude, ϕ (radians) and Julian day, t, following the solar geometry model of Brock (1981):

$$n_{\mathrm{h}}(\phi, t) = \frac{2}{15} \cdot \arccos\left[-\tan(\phi) \cdot \tan(\delta(t))\right] \cdot \frac{360}{2\pi}, \tag{5}$$

where $\delta(t)$ is the solar declination angle (in radians) and is given by:

$$\delta(t) = 23.45 \cdot \sin\left(\frac{2\pi \cdot (284 + t)}{365}\right) \cdot \frac{2\pi}{360}. \tag{6}$$

Prescribed PAR_0 is attenuated with depth following the Beer–Lambert law:

$$\mathrm{PAR}(z) = \mathrm{PAR}_0 \cdot e^{-(k_{\mathrm{PAR}} \cdot z)}, \tag{7}$$

where k_{PAR} (m^{-1}) is the PAR attenuation coefficient and is calculated following Morel et al. (2007) as a single value for the euphotic zone as a function of prescribed MLD and the diffuse attenuation coefficient at 490 nm, $k_\mathrm{d}(490)$:

$$k_\mathrm{PAR} = 0.0864 \cdot 0.884 \cdot k_\mathrm{d}(490) - 0.00137 \cdot \left(k_\mathrm{d}(490)\right)^{-1}, \quad \text{if MLD} \leq \left(k_\mathrm{d}(490)\right)^{-1}, \tag{8a}$$

$$k_\mathrm{PAR} = 0.0665 \cdot 0.874 \cdot k_\mathrm{d}(490) - 0.00121 \cdot \left(k_\mathrm{d}(490)\right)^{-1}, \quad \text{if MLD} > \left(k_\mathrm{d}(490)\right)^{-1}, \tag{8b}$$

where $k_\mathrm{d}(490)$ is derived from prescribed Chl$a$ using the Case 1 water regression of Morel (1988):

$$k_\mathrm{d}(490) = 0.0166 + 0.07242 \cdot \mathrm{Chla}^{0.68955}. \tag{9}$$

The euphotic zone depth z_eu is defined as the depth at which PAR decreases to 0.1% of its surface value (as recommended by Buesseler et al., 2020).

Text S3. Observational Datasets for Model Optimisation

We use observational data from six contrasting oceanographic sites that host, or have hosted, long-term time-series programs on particulate fluxes, following Rufas, Khatiwala, Bisson, Martin, and Bouman (2025): HOT/ALOHA (Hawaii Ocean Time-series station ALOHA); BATS/OFP (Bermuda Atlantic Time-Series/Oceanic Flux Program site); EqPac (U.S. Joint Global Ocean Flux Study Equatorial Pacific process study site); PAP-SO (Porcupine Abyssal Plain time-Series Observatory); OSP (Ocean Station Papa); and HAUSGARTEN (the Long-Term Ecological Research observatory HAUSGARTEN). Together, these sites span a broad range of productivity regimes across distinct biogeographical provinces: from oligotrophic subtropical gyres with persistently low productivity (HOT/ALOHA, BATS/OFP), to productive subpolar systems with strong seasonality and recurrent spring and autumn phytoplankton blooms (PAP-SO, OSP), to high-productivity equatorial upwelling zones with sustained year-round productivity (EqPac), to high-latitude polar environments where productivity is lower overall and peaks during the summer months (HAUSGARTEN).

For these six sites, we obtained three types of observational constraints: (i) *in situ* flux measurements of POC, PIC, and bSi derived from sediment traps and radionuclide disequilibria (mainly ^{234}Th, but also ^{210}Po, ^{228}Th, and ^{230}Th); (ii) *in situ* particle imagery from the Underwater Vision Profiler 5 (UVP5), providing particle number concentrations and particle size distributions; (iii) satellite-based estimates of POC export flux. Each observational approach has distinct advantages. Sediment traps, which physically intercept sinking particles, provide the most direct estimates of fluxes and are widely considered the gold standard for flux collection (e.g., Buesseler et al., 2007; Le Moigne et al., 2013).

Radionuclide disequilibria, by contrast, allow fluxes to be inferred from standard water sampling methods (e.g., Conductivity, Temperature, and Depth (CTD) deployments) during a single sampling event, enabling higher spatial resolution and more logistically efficient broad-scale surveys, as opposed to time-series measurements at single points. UVP5 imagery offers the most direct observations of particle size structure in the upper 2000 m of the water column. In contrast, satellite-based export estimates are indirect and surface-limited, and are used primarily as a consistency check in this study.

In Situ Particulate Flux Data

SLAMS-2.0 has been optimised using *in situ* observational data of POC flux from sediment traps and radionuclide disequilibria compiled by Rufas et al. (2025), along with newly compiled PIC and bSi flux data from the same set of 72 sources (**Figure S4**, and Table S8 in Rufas et al., 2025). Our six study locations were selected for their availability of concurrent measurements of POC, PIC, and bSi flux in a time-series fashion. The data span 1978–2022 and include long-term time-series, annual process studies, and short-term sampling campaigns.

Because flux collection is generally limited to a few discrete depths, we selected four depth horizons for model–data comparison that capture the main remineralisation zone of POC flux: the base of the euphotic zone (export depth), the upper and lower mesopelagic, and the base of the mesopelagic zone (sequestration depth) (**Table S2** for site-specific depths). This yields a potential of up to 864 observational constraints across tracers, depths, months, and sites.

From the calculated euphotic zone depth (z_{eu}; **Text S2**), a ±10% depth margin was applied to account for uncertainty (after McKinna et al., 2019). Observed fluxes were matched to depths within this range using a flexible window to accommodate measurement variability, according to three scenarios: (i) a single matching depth was expanded by an extra ±10% to reduce reliance on a single measurement/research project/collection method; (ii) if multiple depths matched, the window was adjusted to span from the shallowest to the deepest matching depth; (iii) if no depths fell within the range, the nearest depth shallower than 200 m was used, initially searching within ±20% of z_{eu}, then applying (i) or (ii) to define the final bounds. These adjusted ranges (**Table S2**) were also used to extract modelled fluxes.

Mesopelagic depth zones (upper, lower, base) were defined according to the distribution of flux measurements at each site, generally targeting 300, 600, and 1000 m, and defining windows of ∼20 m around the nearest sediment trap depth. Notably, at HOT/ALOHA and BATS/OFP, the base of mesopelagic zone extends beyond the conventional 1000 m depth, reaching 1500 m, due to the absence of sediment traps between 500–1500 (BATS/OFP) and 800–1500 m (HOT/ALOHA). These mesopelagic depth zones were likewise applied to extract fluxes from the model outputs.

Data were quality-controlled prior to analysis. Fluxes were log-transformed to account for their known log-normal distribution (e.g., Cael et al., 2021) and then filtered using the interquartile range (IQR) method: the first and third quartiles were calculated, and any value falling outside a conservative threshold of 3 × IQR was flagged as an outlier. Only one outlier was identified: a PIC flux measurement at OSP at the base of the euphotic zone, derived from radionuclide estimates from the EXPORTS campaign (in Roca-Martí et al., 2021), which was over an order of magnitude lower than the long-term sediment trap record at the same site from Wong, Waser, Whitney, Johnson, and Page

(2002). Additionally, we excluded monthly flux profiles with fewer than two observations. After filtering, the dataset comprised 565 climatological mean data points (**Figure S5**). Inspection of **Figure S5A** shows that peak POC fluxes increase from subtropical to equatorial and subpolar sites, before declining again at the polar site. Each site displays a distinct particulate flux regime, explained below.

In the subtropical gyres (HOT/ALOHA and BATS/OFP), export fluxes are modest year-round ($\sim$20–30 $\mathrm{mg\,C\,m^{-2}\,d^{-1}}$), with HOT/ALOHA more stable and BATS/OFP showing occasional peaks ($\sim$60 $\mathrm{mg\,C\,m^{-2}\,d^{-1}}$ in March) (**Figure S5A**). POC flux attenuates sharply within the upper mesopelagic, over an order of magnitude, consistent with warm, low-productivity waters that have high remineralisation rates (Martin et al., 1987; Conte, Maureen et al., 2001; Marsay et al., 2015). Corresponding PIC:POC flux ratios at the base of mesopelagic (**Figure S6A**) are relatively high at BATS/OFP ($>$1.0) but low at HOT/ALOHA ($<$0.5), while Si:POC flux ratios (**Figure S6B**) remain very low at HOT/ALOHA ($\sim$0.04) and moderately low at BATS/OFP ($\sim$0.30). This indicates carbonate-rich coccolithophore export with little diatom contribution, supported by local observations during the VERTIGO program (Lamborg et al., 2008) and the OFP time-series (Conte et al., 2019).

At the equatorial upwelling site (EqPac), episodic export pulses exceed 250 $\mathrm{mg\,C\,m^{-2}\,d^{-1}}$ (**Figure S5A**), interspersed with long periods of low or missing data, likely reflecting variability in upwelling and El Niño/Southern Oscillation cycles (Kawahata & Gupta, 2003). Although POC flux attenuates strongly with depth, sequestration fluxes remain relatively high (annual mean $\sim$5 $\mathrm{mg\,C\,m^{-2}\,d^{-1}}$). High sequestration depth PIC:POC ($>$1.0) (**Figure S6A**) and moderate-to-high Si:POC ($\sim$0.6) (**Figure S6B**) suggest mixed coccolithophore–diatom export (Arteaga & Rousseaux, 2023), with carbonates relatively well-preserved at depth.

In the subpolar North Atlantic and Pacific, PAP-SO and OSP both exhibit strong bloom-driven seasonality, with spring export peaks exceeding 150 $\mathrm{mg\,C\,m^{-2}\,d^{-1}}$ (**Figure S5A**). Export at PAP-SO penetrates more effectively to depth, but annual sequestration flux is higher at OSP ($\sim$5 vs. $\sim$3 $\mathrm{mg\,C\,m^{-2}\,d^{-1}}$) (**Figure S5A**). Both sites are characterised by low mid-water PIC:POC ratios ($\sim$0.10 at PAP-SO; $\sim$0.40 at OSP), reflecting weak calcification (**Figure S6A**). However, at sequestration depth Si:POC diverges: PAP-SO remains relatively low ($\sim$0.30), whereas OSP is high ($\sim$0.90), indicating stronger diatom control at OSP (**Figure S6B**). Both sites have a mixed community dominated by diatoms in the spring bloom that transitions to coccolithophores later in spring (Boyd & Harrison, 1999; Lampitt et al., 2023).

Finally, at the polar site HAUSGARTEN, export fluxes are low for most of the year ($<$15 $\mathrm{mg\,C\,m^{-2}\,d^{-1}}$), punctuated by short, intense summer pulses ($\sim$35 $\mathrm{mg\,C\,m^{-2}\,d^{-1}}$) that sink efficiently to depth (**Figure S5A**). PIC:POC ratios at the base of mesopelagic remain low (annual mean $\sim$0.30) (**Figure S6A**) and Si:POC is quite modest ($\sim$0.23) (**Figure S6B**), pointing to a short productive season dominated by diatom-rich communities associated with sea-ice retreat and light availability (Hop et al., 2006; Nöthig et al., 2015).

In summary, the combined mineral-to-POC ratios support the idea that carbonate-rich export (coccolithophores) dominates in oligotrophic subtropical gyres (BATS/OFP, HOT/ALOHA), while biogenic silica-rich export (diatoms) is more important in the high-nutrient regions of high-latitude (PAP-SO, OSP, HAUSGARTEN) and upwelling (EqPac) systems. Deep-water (sequestration depth) combined mineral-to-POC ratios further suggest that diatom-derived silica is relatively well-preserved in the Pacific Ocean sites (EqPac, OSP) compared to subtropical gyres and the Atlantic Ocean sites, while carbonate preservation appears stronger at the Atlantic sites (BATS/OFP, PAP-SO) and EqPac but weaker in most high-latitude systems. These patterns are consistent with the 'Silicate Ocean' versus 'Carbonate Ocean' framework at the mesopelagic/bathypelagic boundary proposed by Honjo, Manganini, Krishfield, and Francois (2008).

In Situ Particle Imaging Data

UVP5 data were compiled by Kiko et al. (2022) and we extracted them from the EcoPart repository (`https://ecopart.obs-vlfr.fr`) following the procedure in Figure S4 in Rufas et al. (2025). UVP5-based observations of particle number concentration span the period 2008–2021 and are binned into 16 particle size classes, consistent with SLAMS-2.0. While valuable for characterising particle size structure, we note some caveats with these data: they represent instantaneous snapshots rather than time-integrated measurements, as sediment traps do; uncertainty estimates are not provided by the EcoTaxa platform, and may be substantial; and the UVP5 cannot detect particles smaller than 100 μm, which constitute the majority of particles.

Satellite-Based Estimates of POC Export Flux

Satellite-based estimates of POC export flux (i.e., at the base of the euphotic zone) were obtained from ESA's BICEP project (Jönsson et al., 2022). These have been derived globally using three established export production algorithms (Dunne et al., 2005; Henson et al., 2011; Z. Li & Cassar, 2016) driven by satellite observations of sea surface temperature (SST) (GHRSST/OSTIA, UK Met Office, 2005), Chl$a$ and the diffuse attenuation coefficient at 490 nm (OC-CCI, Sathyendranath et al., 2020), and NPP (BICEP, Kulk et al., 2021).

These algorithms differ in their structure and data sources: Dunne et al. (2005)'s is based on a statistical fit to SST and a phytoplankton productivity metric (either NPP or Chl*a* normalised by euphotic depth) after a global compilation of POC flux export measurements from a combination of shallow sediment traps and ^{234}Th-derived POC fluxes, with outputs constrained within fixed bounds; Henson et al. (2011) uses a simpler exponential fit to SST and NPP using observations of ^{234}Th-derived fluxes from various authors, and is parameterised for export at $\sim$100 m depth, without explicitly incorporating euphotic depth; and Z. Li and Cassar (2016) applies a machine-learning approach (genetic programming) to optimise the empirical relationship between NPP and SST of Henson et al. (2011) and Laws, Falkowski, Smith, Ducklow, and McCarthy (2000), aiming to better match dissolved O_2:Ar-based estimates of net community production, and improve predictive skill over earlier empirical formulations.

Figure S7 presents a validation of these three satellite-based BICEP products estimating POC export flux against our *in situ* dataset from sediment traps and radionuclides. The BICEP-Li product outperforms both the BICEP-Henson and BICEP-Dunne algorithms, as indicated by its higher Spearman rank correlation coefficient (ρ) and lower bias (δ) and root mean square error (RMSE). In contrast, BICEP-Henson and BICEP-Dunne tend to systematically underestimate *in situ* measurements (negative δ), particularly at high flux values, whereas BICEP-Li more accurately captures the magnitude of observed high export peaks.

Text S4. Particle State Equations

We present the Lagrangian superparticle state equations governing particle attributes (fractal scaling, stickiness, and sinking velocity). Parameters are given in **Tables A1–A3** and prescribed variables in **Texts S1–S2**. While many equations are inherited from SLAMS-1.0, some have been extended or modified to reflect the updated process representations in SLAMS-2.0.

Modelled aggregates form through the coagulation of idealised spherical primary particles (sphericity of primaries is a necessary simplification for hydrodynamic calculations, but in reality are irregular in shape). The resulting aggregates are fractal structures: porous, irregular, and statistically self-similar across scales. This self-similarity implies a scaling relationship between size-dependent properties (mass, area, length) and a characteristic scale (radius, diameter). For marine aggregates, the relevant property that scales with size is mass, m_{p} —or, equivalently the number of primary particles, n_{pp}— following a power law, rather than the cubic relation of a compact sphere:

$$m_{\mathrm{p}}^{\mathrm{fractal}} = m_{\mathrm{pp}} \cdot n_{\mathrm{pp}} = m_{\mathrm{pp}} \cdot \left(\frac{r_{\mathrm{p}}}{r_{\mathrm{pp}}}\right)^{D_3}, \tag{10a}$$

$$m_{\mathrm{p}}^{\mathrm{compact}} = \rho_{\mathrm{p}} \cdot V_{\mathrm{p}} = \rho_{\mathrm{p}} \cdot \frac{4\pi}{3} \cdot r_{\mathrm{p}}^{3}, \tag{10b}$$

where m_{pp} and r_{pp} are the mass and radius of the primary particles, V_{p} is the bulk (envelope) volume of the aggregate, ρ_{p} its bulk density, and D_3 the three-dimensional (3-D) fractal dimension. The fractal dimension quantifies how efficiently an object fills space: $D_3 = 1$ for filamentary (one-dimensional) structures, $D_3 = 2$ for surface-like (two-dimensional) forms, and $D_3 = 3$ for compact, volumetric (three-dimensional) bodies. For a compact, non-porous sphere, $D_3 = 3$; in contrast, marine aggregates typically exhibit $D_3 \approx$ 1.3–2.6, reflecting their porous structure, in which solid material occupies only a *fraction* of the embedding 3-D space, and the object is therefore *fractal* (Logan & Wilkinson, 1990; Kilps, 1993; X. Li & Logan, 1995; Burd & Jackson, 1997; Jackson et al., 1997). Lower D_3 values correspond to open, highly porous structures and higher values to denser, more compact structures.

In SLAMS-2.0, primary particles are assigned $D_3 = 3$, while newly formed aggregates sample D_3 uniformly within 1.3–1.9 (a range adjusted after Kilps, 1993). From **Eq. 10**, since $m_\mathrm{p} \propto r_\mathrm{p}^{D_3}$ but the volume scales as $V_\mathrm{p} \propto r_\mathrm{p}^3$, aggregates with $D_3 < 3$ gain volume faster than mass as they grow, producing lower bulk density and higher porosity. This behaviour —i.e., large aggregates that are relatively porous and therefore sink more slowly than compact particles of the same size— is a key observation that the fractal scaling in SLAMS-2.0 is designed to capture. Particle attributes are derived following this scaling below.

Particle Attributes Derived from Fractal Scaling

Mass. The dry mass of a particle, m_p (g), is obtained from its material composition:

$$m_\mathrm{p} = \sum_{x=1} q_x \cdot M_x, \quad x = \text{organic matter, CaCO3, bSi, clay}, \tag{11}$$

where q_x is the quantity (mol) of material x and M_x its molar mass. The organic matter component combines organic carbon ($m_{\mathrm{C_{org}}} = q_{\mathrm{C_{org}}} \cdot M_\mathrm{C}$) and TEP carbon ($m_\mathrm{TEPC} = q_\mathrm{TEPC} \cdot M_\mathrm{C}$), converted to their respective organic matter (OM) equivalents via carbon-to-matter factors, i.e., $m_\mathrm{OM} = m_{\mathrm{C_{org}}}/f_\mathrm{C:OM} + m_\mathrm{TEPC}/f_\mathrm{TEPC:TEP}$.

Volume. The solid (non-porous) volume of the aggregate particle, V_p^S (μm^3), is:

$$V_\mathrm{p}^\mathrm{S} = \sum_{x=1} \frac{m_x}{\rho_x}, \tag{12}$$

where ρ_x is the density of each material x.

Radius. The number of constituent primary particles, n_{pp} scales with aggregate radius as r_{p} (μm), as $n_{\mathrm{pp}} = (r_{\mathrm{p}}/r_{\mathrm{pp}})^{D_3}$ (**Eq. 10a**), which can be rearranged to give:

$$r_{\mathrm{p}} = r_{\mathrm{pp}} \cdot {n_{\mathrm{pp}}}^{1/D_3}. \tag{13}$$

For $D_3 < 3$, aggregates have a more open structure and therefore larger radii for a given n_{pp}. The fractal scaling assumes identical, spherical primary particles of radius:

$$r_{\mathrm{pp}} = \left(\frac{3 \cdot V_{\mathrm{pp}}}{4\pi}\right)^{1/3}, \tag{14}$$

where $V_{\mathrm{pp}} = V_{\mathrm{p}}^{\mathrm{S}}/n_{\mathrm{pp}}$ is the volume of a single primary particle.

Porosity. Let $V_{\mathrm{p}}^{\mathrm{B}}$ denote the bulk (envelope) volume of a aprticle. Porosity, P_{p}, is defiend as the fraction of the particle volume occupied by seawater:

$$P_{\mathrm{p}} = 1 - \frac{V_{\mathrm{p}}^{\mathrm{S}}}{V_{\mathrm{p}}^{\mathrm{B}}} = 1 - \frac{n_{\mathrm{pp}} \cdot V_{\mathrm{pp}}}{V_{\mathrm{p}}^{\mathrm{B}}} = 1 - n_{\mathrm{pp}} \cdot \left(\frac{r_{\mathrm{pp}}}{r_{\mathrm{p}}}\right)^3. \tag{15}$$

Substituting the fractal relation for n_{pp} (**Eq. 10a**) yields:

$$P_{\mathrm{p}} = 1 - \left(\frac{r_{\mathrm{p}}}{r_{\mathrm{pp}}}\right)^{D_3 - 3}. \tag{16}$$

This expression implies a size-dependent porosity: smaller aggregates are relatively compact, whereas larger aggregates are increasingly porous as the spacing between primary particles grows, increasing the fraction of seawater within the particle structure.

From the porosity, we define the effective radius, $r_{\mathrm{p}}^{\mathrm{eff}}$, as the radius of an equivalent non-porous sphere containing the same volume of solid material as the aggregate:

$$r_{\mathrm{p}}^{\mathrm{eff}} = r_{\mathrm{p}} \cdot (1 - P_{\mathrm{p}})^{1/3}. \tag{17}$$

Thus, while the bulk radius r_{p} characterises the full particle envelope, including porous space, the effective radius $r_{\mathrm{p}}^{\mathrm{eff}}$ represents only the volume of solid material, and is therefore smaller than the bulk radius.

Density. The bulk (effective) density of a particle, ρ_{p} ($\mathrm{g\,cm^{-3}}$), combines the solid and pore water fractions:

$$\rho_{\mathrm{p}} = (1 - P_{\mathrm{p}}) \cdot \rho_{\mathrm{p}}^{\mathrm{S}} + P_{\mathrm{p}} \cdot \rho_{\mathrm{w}}, \tag{18}$$

where ρ_{w} is the prescribed seawater density, and $\rho_{\mathrm{p}}^{\mathrm{S}} = m_{\mathrm{p}}/V_{\mathrm{p}}^{\mathrm{S}}$ is the density of the solid fraction. Finally, the particle's excess density, which is used to calculate its sinking velocity, is defined as:

$$\Delta\rho_{\mathrm{p}} = \rho_{\mathrm{p}} - \rho_{\mathrm{w}}. \tag{19}$$

Particle Stickiness

Stickiness, α_{p} (ranging from 0 to 1), represents the likelihood that two particles will attach upon collision. In the ocean, particles do not always stick upon contact: some collisions result in attachment, while others do not. This tendency to stick is enhanced in the presence of organic matter, particularly transparent exopolymer particles (TEPs), which act as natural 'glues' that promote aggregation (Alldredge et al., 1993).

TEPs are carbohydrate-based gels cross-linked by divalent cations and sulfate bridges (Passow, 2002; Meng & Liu, 2016) and are the driver of stickiness in the SLAMS formulation. Empirical studies typically infer stickiness from aggregation experiments involving the presence of TEPs (Kiørboe & Hansen, 1993; Dam & Drapeau, 1995; Engel, 2000). Although no exact formula exists for predicting stickiness directly from TEP concentration, Jokulsdottir and Archer (2016) introduced a mechanistic representation in SLAMS-1.0 linking higher TEP content to an increased probability of particle attachment. In their framework, stickiness increases linearly with the fraction of an aggregate's solid volume occupied by TEP material:

$$\alpha_{\mathrm{p}} = \frac{m_{\mathrm{TEP}}/\rho_{\mathrm{TEP}}}{V_{\mathrm{p}}^{\mathrm{S}}} = \frac{V_{\mathrm{TEP}}}{V_{\mathrm{p}}^{\mathrm{S}}}. \tag{20}$$

where $V_{\mathrm{TEP}} = m_{\mathrm{TEP}}/\rho_{\mathrm{TEP}}$ is the TEP volume within the aggregate.

While **Eq. 20** provides a simple and physically intuitive formulation, it may not capture all aspects of particle adhesion. We hypothesise that stickiness increases with TEP content up to a saturation point, beyond which additional polymer yields diminishing gains in adhesive contact area, analogous to saturating responses observed in other biogeochemical processes. In addition, mineral content may reduce effective adhesion by occupying surface area and introducing rigid contacts that oppose gel-mediated bridging. Based on these two considerations, SLAMS-2.0 includes an alternative formulation in which stickiness depends on (i) a saturating (Michaelis–Menten) response to the TEP volume fraction and (ii) a multiplicative mineral dilution factor that reduces stickiness in proportion to the mineral fraction:

$$\alpha_{\mathrm{p}} = \underbrace{\frac{\dfrac{V_{\mathrm{TEP}}}{V_{\mathrm{p}}^{\mathrm{S}}}}{\dfrac{V_{\mathrm{TEP}}}{V_{\mathrm{p}}^{\mathrm{S}}} + k_{\mathrm{TEP}}}}_{\text{TEP saturation}} \cdot \underbrace{\left(1 - \frac{V_{\mathrm{mineral}}}{V_{\mathrm{p}}^{\mathrm{S}}}\right)}_{\text{mineral dilution}}, \tag{21}$$

where $V_{\mathrm{TEP}}/V_{\mathrm{p}}^{\mathrm{S}}$ is the dimensionless TEP volume fraction (0–1), k_{TEP} is the half-saturation constant (dimensionless; equals the TEP fraction at which the TEP term reaches 0.5), $V_{\mathrm{mineral}}/V_{\mathrm{p}}^{\mathrm{S}}$ is the mineral volume fraction (0-1).

Particle Sinking Velocity

The particle sinking velocity, v_{p} ($\mathrm{m\,d^{-1}}$), follows from a balance of three forces on a sphere falling in viscous fluid (e.g., Maggi, 2013): downward gravitational force, F_{g}, upward buoyancy force that emerges from the weight of the fluid displaced by the particle,

F_{b}, and drag force that pulls the particle upward, F_{d}:

$$F_{\mathrm{g}} = m_{\mathrm{p}} \cdot g = \rho_{\mathrm{p}} \cdot V_{\mathrm{p}}^{\mathrm{B}} \cdot g, \tag{22a}$$

$$F_{\mathrm{b}} = m_{\mathrm{w}} \cdot g = \rho_{\mathrm{w}} \cdot V_{\mathrm{p}}^{\mathrm{B}} \cdot g, \tag{22b}$$

$$F_{\mathrm{d}} = \frac{1}{2} \cdot \rho_{\mathrm{w}} \cdot v_{\mathrm{p}}^2 \cdot C_{\mathrm{D}} \cdot A_{\mathrm{p}}, \tag{22c}$$

where g is the gravitational constant, $V_{\mathrm{p}}^{\mathrm{B}} = (4/3) \cdot \pi \cdot r_{\mathrm{p}}^3$ is the particle (bulk) volume, $A_{\mathrm{p}} = \pi \cdot r_{\mathrm{p}}^2$ is the projected area of the particle, and C_{D} is the drag coefficient.

When the two retarding forces balance the gravitational force, the net force acting on the particle vanishes ($F_{\mathrm{net}} = F_{\mathrm{g}} - (F_{\mathrm{b}} + F_{\mathrm{d}}) = 0$) and, consequently, the net acceleration of the particle goes to zero, so it keeps falling at a constant velocity, its terminal velocity (v_{p}). Its generic expression can be isolated from the force balance F_{net}:

$$v_{\mathrm{p}} = \sqrt{\frac{8}{3}\frac{r_{\mathrm{p}} \cdot g \cdot \Delta\rho_{\mathrm{p}}}{\rho_{\mathrm{w}} \cdot C_{\mathrm{D}}}}. \tag{23}$$

The drag coefficient, C_{D}, is a function of the flow regime around the particle, and is parameterised through the Reynolds number, Re (dimensionless):

$$Re = \frac{\text{inertial force}}{\text{viscous force}} = \frac{d_{\mathrm{p}} \cdot v_{\mathrm{p}} \cdot \rho_{\mathrm{w}}}{\mu}, \tag{24}$$

where v_{p} is in $\mathrm{m\,s^{-1}}$, $d_{\mathrm{p}} = 2 \cdot r_{\mathrm{p}}$ is the particle diameter in metres, ρ_{w} is the prescribed seawater density in $\mathrm{kg\,m^{-3}}$, and μ is the prescribed seawater dynamic viscosity in $\mathrm{kg\,m^{-1}\,s^{-1}}$. Re compares inertial to viscous forces: low values ($Re < 0.1$) indicates viscous-dominated (laminar) flow, whereas larger values indicate transitional or turbulent flow (e.g., caused by increasing particle size or settling velocity). Although no exact analytical relationship exists between Re and C_{D}, several empirical correlations for impermeable spheres are widely used (e.g., Maggi, 2013; Laurenceau-Cornec et al., 2019). SLAMS-2.0 adopts the empirical formulation of White (1974) for solid spheres, which uses the Stokes (1851) drag in laminar flow and an extended fit for higher Re:

$$C_\mathrm{D} = \frac{24}{Re}, \qquad Re < 0.1 \quad \text{(laminar)} \tag{25a}$$

$$C_\mathrm{D} = \frac{24}{Re} + \frac{6}{1+\sqrt{Re}} + 0.4, \qquad Re \geq 0.1 \quad \text{(transitional/turbulent)} \tag{25b}$$

These drag relations yield two corresponding expressions for v_p (in $\mathrm{m\,s^{-1}}$): one for laminar flow (known as the 'Stokes' velocity', after Stokes, 1851) and another for transitional/turbulent flow:

$$v_\mathrm{p} = \frac{2}{9}\,\frac{g \cdot \Delta\rho_\mathrm{p} \cdot r_\mathrm{p}^2}{\mu}, \qquad \text{(laminar)} \tag{26a}$$

$$v_\mathrm{p} = \sqrt{\frac{4}{3}\,\frac{g \cdot \Delta\rho_\mathrm{p} \cdot d_\mathrm{p}}{\rho_\mathrm{w} \cdot C_\mathrm{D}}}, \qquad \text{(transitional/turbulent)} \tag{26b}$$

According to the expression for laminar flow, v_p increases linearly with excess density and quadratically with particle radius, implying a parabolic rise in velocity with particle size. This form is commonly used to compute sinking velocities, but it relies on three simplifying assumptions: (i) laminar flow ($Re < 0.1$); (ii) impermeable, non-fractal particles; and (iii) perfectly spherical geometry. By contrast, for transitional/turbulent flow, C_D and Re both depend on v_p, so the velocity must be solved iteratively. In SLAMS-2.0, this is achieved using a Newton iteration method until convergence.

Text S5. Mesozooplankton Size-Dependent Attributes

In SLAMS-2.0, several mesozooplankton traits relevant to encounter dynamics are parameterised explicitly as functions of body size. Mesozooplankton are represented by discrete size classes indexed by j, each characterised by a representative equivalent spherical diameter (ESD). The characteristic diameter of each size class is defined as the geometric mean of the bin bounds (i.e., the middle point),

$$\mathrm{ESD}_j^{\mathrm{geom}} = \sqrt{\mathrm{ESD}_j^{\mathrm{lower}} \cdot \mathrm{ESD}_j^{\mathrm{upper}}}, \tag{27}$$

where 'lower' and 'upper' denote the lower and upper bounds of size class j. As explained in Appendix A23 (after Kwong & Pakhomov, 2021, Table S1), there are 26 size classes, with bounds ranging 185–10,950 μm, increasing by a constant factor of 1.17.

Radius. The characteristic radius of zooplankton size class j is:

$$r_{\mathrm{z},j} = \frac{\mathrm{ESD}_j^{\mathrm{geom}}}{2}. \tag{28}$$

Prosome length. Prosome length is estimated from ESD assuming a prolate spheroidal body shape with aspect ratio 0.38, following Kiørboe (2011):

$$\mathrm{PL}_{\mathrm{z},j} = \frac{\mathrm{ESD}_j^{\mathrm{geom}}}{0.38^{2/3}}. \tag{29}$$

Wet weight quota. Each size class is assigned a characteristic wet mass, $m_{\mathrm{z},j}$ (mg WW), computed from the radius assuming spherical geometry and a constant body density of $\rho_{\mathrm{z}} = 1\ \mathrm{g\,cm^{-3}}$ (after Kiørboe, 2013):

$$m_{\mathrm{z},j} = \rho_{\mathrm{z}} \cdot \frac{4\pi}{3} \cdot {r_{\mathrm{z},j}}^3, \tag{30}$$

Carbon weight quota. Wet mass, $m_{\mathrm{z},j}$ (mg WW), is converted to carbon mass, $m_{\mathrm{C},j}$ (mg C), using the empirical copepod relationship of Kiørboe (2013, Table 2):

$$\log_{10}(m_{\mathrm{z},j}) = -0.93 + 0.95 \cdot \log_{10}(m_{\mathrm{C},j}). \tag{31}$$

Reaction distance. The effective reaction distance governing particle–zooplankton encounters is given by:

$$r_{\mathrm{z}_j}^{\mathrm{detect}} = R_{\mathrm{z}} \cdot r_{\mathrm{z},j}, \tag{32}$$

where R_{z} is a dimensionless parameter describing mechanoreceptive or chemical sensing efficiency (Table **??**).

Swimming speed. For cruising mesozooplankton, swimming speed, $v_{\mathrm{z},j}$ ($\mathrm{m\,s^{-1}}$), follows the empirical size-based formulation of Kiørboe (2011, Fig. 3):

$$\log_{10}(v_{\mathrm{z},j}) = 0.39 + 0.79 \cdot \log_{10}(\mathrm{ESD}_j^{\mathrm{geom}}), \tag{33}$$

where $v_{\mathrm{z},j}$ is expressed in $\mathrm{cm\,s^{-1}}$ and $\mathrm{ESD}_j^{\mathrm{geom}}$ in cm.

Faecal pellet volume. Faecal pellet volume depends on the PL of the mesozooplankton (**Eq. 29**), with a relationship given by the empirical formula of Stamieszkin et al. (2015):

$$\log_{10}(V_{\mathrm{fp}}^{\mathrm{B}}) = 5.4 + 2.58 \cdot \log_{10}(\mathrm{PL}_{\mathrm{z},j}), \tag{34}$$

where $V_{\mathrm{fp}}^{\mathrm{B}}$ is in $\mu\mathrm{m}^3$ and $\mathrm{PL}_{\mathrm{z},j}$ is in mm.

Gut volume. The mesozooplankter gut volume is estimated from the bulk volume of faecal pellets that could be egested from the ingested food particle. As per Jansen (2001, Table 1, footnote), a good approximation is:

$$V_{\mathrm{gut}} = 5 \cdot V_{\mathrm{fp}}^{\mathrm{B}}. \tag{35}$$

References

Alldredge, A. L., Passow, U., & Logan, B. E. (1993). *The abundance and significance of a class of large, transparent organic particles in the ocean* (Vol. 40) (No. 6). doi: 10.1016/0967-0637(93)90129-Q

Arteaga, L., & Rousseaux, C. (2023). Impact of Pacific Ocean heatwaves on phytoplankton community composition. *Communications Biology*, *6*. doi: 10.1038/s42003-023-04645-0

Aumont, O., Ethé, C., Tagliabue, A., Bopp, L., & Gehlen, M. (2015). PISCES-v2: An ocean biogeochemical model for carbon and ecosystem studies. *Geoscientific Model Development*, *8*(8), 2465–2513. doi: 10.5194/gmd-8-2465-2015

Bates, N. R., Johnson, R. J., Lopez, P. Z., Hayden, M., May, R., Derbyshire, L., … Smith, D. (2023). *Determination of carbon, nitrogen, and phosphorous content in sinking particles at the Bermuda Atlantic Time-series Study (BATS) site from 1988-2022 using a Particle Interceptor Trap System (PITS), Version 1 [dataset].* doi: 10.26008/1912/bco-dmo.894099.1

Behrenfeld, M. J., & Falkowski, P. G. (1997). Photosynthetic rates derived from satellite-based chlorophyll concentration. *Limnology and Oceanography*, *42*(1), 1–20. doi: 10.4319/lo.1997.42.1.0001

Booth, B. C. (1988). Size classes and major taxonomic groups of phytoplankton at two locations in the subarctic Pacific Ocean in May and August, 1984. *Marine Biology*, *97*, 275–286. doi: 10.1007/BF00391313

Boyd, P., & Harrison, P. J. (1999). Phytoplankton dynamics in the NE subarctic Pacific. *Deep-Sea Research II*, *46*(11-12), 2405–2432. doi: 10.1016/S0967-0645(99)00069-7

Brock, T. D. (1981). Calculating solar radiation for ecological studies. *Ecological Modelling*, *14*, 1–19. doi: 10.1016/0304-3800(81)90011-9

Buesseler, K. O., Boyd, P. W., Black, E. E., & Siegel, D. A. (2020). Metrics that matter for assessing the ocean biological carbon pump. *Proceedings of the National Academy of Sciences*, *117*(18), 9679–9687. doi: 10.1073/pnas.1918114117

Buesseler, K. O., Lamborg, C. H., Boyd, P. W., Lam, P. J., Trull, T. W., Bidigare, R. R., ... Wilson, S. (2007). Revisiting carbon flux through the ocean's twilight zone. *Science*, *316*, 567–570. doi: 10.1126/science.113795

Burd, A. B., & Jackson, G. A. (1997). Predicting particle coagulation and sedimentation rates for a pulsed input. *Journal of Geophysical Research*, *102*, 10545–10561. doi: 10.1029/96JC03592

Cael, B. B., Bisson, K. M., Conte, M., Duret, M. T., Follett, C. L., Henson, S. A., ... Talmy, D. (2021). Open ocean particle flux variability from surface to seafloor. *Geophysical Research Letters*, *48*(9). doi: 10.1029/2021GL092895

Carr, M.-E. (2002). Estimation of potential productivity in Eastern Boundary Currents using remote sensing. *Deep-Sea Research II*, *49*(1-3), 59–80. doi: 10.1016/S0967-0645(01)00094-7

Conte, M., Carter, A. M., Koweek, D. A., Huang, S., & Weber, J. C. (2019). The elemental composition of the deep particle flux in the Sargasso Sea. *Chemical Geology*, *511*, 279–313. doi: 10.1016/j.chemgeo.2018.11.001

Conte, Maureen, H., Ralph, N., & Ross, E. H. (2001). Seasonal and interannual variability in deep ocean particle fluxes at the Oceanic Flux Program (OFP)/Bermuda Atlantic Time Series (BATS) site in the western Sargasso Sea near Bermuda. *Deep-*

Sea Research II, *48*(8-9), 1471–1505. doi: 10.1016/S0967-0645(00)00150-8

Dam, H. G., & Drapeau, D. T. (1995). Coagulation efficiency, organic-matter glues and the dynamics of particles during a phytoplankton bloom in a mesocosm study. *Deep-Sea Research II*, *42*(1), 111–123. doi: 10.1016/0967-0645(95)00007-D

De Boyer Montégut, C., Madec, G., Fischer, A. S., Lazar, A., & Iudicone, D. (2004). Mixed layer depth over the global ocean: an examination of profile data and a profile-based climatology. *Journal of Geophysical Research*, *109*, C12003. doi: 10.1029/2004JC002378

Dunne, J. P., Armstrong, R. A., Gnanadesikan, A., & Sarmiento, J. L. (2005). Empirical and mechanistic models for the particle export ratio. *Global Biogeochemical Cycles*, *19*(4), GB4026. doi: 10.1029/2004GB002390

Engel, A. (2000). The role of transparent exopolymer particles (TEP) in the increase in apparent particle stickiness (alpha) during the decline of a diatom bloom. *Journal of Plankton Research*, *22*(3), 485–497. doi: 10.1093/plankt/22.3.485

Giesbrecht, K. E., Hamme, R. C., & Emerson, S. R. (2012). Biological productivity along Line P in the subarctic northeast Pacific: In situ versus incubation-based methods. *Global Biogeochemical Cycles*, *26*(3). doi: https://doi.org/10.1029/2012GB004349

Henson, S. A., Sanders, R. J., & Madsen, E. (2012). Global patterns in efficiency of particulate organic carbon export and transfer to the deep ocean. *Global Biogeochemical Cycles*, *26*(1). doi: 10.1029/2011GB004099

Henson, S. A., Sanders, R. J., Madsen, E., Morris, P. J., Le Moigne, F. A., & Quartly, G. D. (2011). A reduced estimate of the strength of the ocean's biological carbon pump. *Geophysical Research Letters*, *38*(4), L04606. doi: 10.1029/2011GL046735

Honjo, S., Manganini, S. J., Krishfield, R. A., & Francois, R. (2008). Particulate organic carbon fluxes to the ocean interior and factors controlling the biological pump: A synthesis of global sediment trap programs since 1983. *Progress in Oceanography*, *76*(3), 217–285. doi: 10.1016/j.pocean.2007.11.003

Hop, H., Falk-Petersen, S., Svendsen, H., Kwasniewski, S., Pavlov, V., Pavlova, O., & Søreide, J. E. (2006). Physical and biological characteristics of the pelagic system across Fram Strait to Kongsfjorden. *Progress in Oceanography*, *71*(2-4), 182–231. doi: 10.1016/j.pocean.2006.09.007

Jackson, G. A. (2001). Effect of coagulation on a model planktonic food web. *Deep-Sea Research I*, *48*(1), 95–123. doi: 10.1016/S0967-0637(00)00040-6

Jackson, G. A. (2004). *Notes on a simple coagulation model — last update 4 January 2004.* Texas.

Jackson, G. A., Maffione, R., Costello, D. K., Alldredge, A. L., Logan, B. E., & Dam, H. G. (1997). Particle size spectra between 1 um and 1 cm at Monterey Bay determined using multiple instruments. *Deep-Sea Research I*, *44*(11), 1739–1767. doi: 10.1016/S0967-0637(97)00029-0

Jansen, H. (2001). *Modelling the marine carbonate pump and its implications on the atmospheric CO2 concentration* (Doctoral Thesis). Universität Bremen.

Jansen, H., Zeebe, R. E., & Wolf-Gladrow, D. A. (2002). Modeling the dissolution of settling CaCO3 in the ocean. *Global Biogeochemical Cycles*, *16*(2), 1027. doi: 10.1029/2000gb001279

Jokulsdottir, T., & Archer, D. E. (2016). A stochastic, Lagrangian model of sinking biogenic aggregates in the ocean (SLAMS 1.0): Model formulation, validation and sensitivity. *Geoscientific Model Development*, *9*(4), 1455–1476. doi: 10.5194/gmd-9-1455-2016

Jönsson, B. F., Sathyendranath, S., Kulk, G., & Dall'Olmo, G. (2022). *BICEP/NCEO: Monthly global Oceanic Export Production, between 1998-2019 at 9 km resolution (derived from the Ocean Colour Climate Change Initiative v4.2 dataset) [dataset].* NERC EDS Centre for Environmental Data Analysis. doi: 10.5285/a6fc730d88fd4935b59d64903715d891

Journet, E., Desboeufs, K. V., Caquineau, S., & Colin, J. L. (2008). Mineralogy as a critical factor of dust iron solubility. *Geophysical Research Letters*, *35*(7), L07805. doi: 10.1029/2007GL031589

Karl, D. M., Letelier, R. M., Bidigare, R. R., Björkman, K. M., Church, M. J., Dore, J. E., & White, A. E. (2021). Seasonal-to-decadal scale variability in primary production and particulate matter export at Station ALOHA. *Progress in Oceanography*, *195*. doi: 10.1016/j.pocean.2021.102563

Kawahata, H., & Gupta, L. P. (2003). El Niño/Southern Oscillation (ENSO) Related Variations in Particulate Export Fluxes in the Western and Central Equatorial Pacific. *Journal of Oceanography*, *59*, 663–670. doi: 10.1023/B:JOCE.0000009595.79408.13

Kawakami, H., Honda, M. C., Matsumoto, K., Fujiki, T., & Watanabe. Shuichi. (2010). East-West distribution of POC fluxes estimated from 234Th in the northern North Pacific in autumn. *Journal of Oceanography*, *66*, 71–83. doi: 10.1007/s10872-010-0006-z

Kiko, R., Picheral, M., Antoine, D., Babin, M., Berline, L., Biard, T., . . . Stemmann,

L. (2022). A global marine particle size distribution dataset obtained with the Underwater Vision Profiler 5. *Earth System Science Data*, *14*(9), 4315–4337. doi: 10.5194/essd-14-4315-2022

Kilps, J. R. (1993). *Fractal dimensions of aggregates formed under natural and engineered fluid environments* (Master of Science). University of Arizona.

Kiørboe, T. (2011). How zooplankton feed: Mechanisms, traits and trade-offs. *Biological Reviews*, *86*(2), 311–339. doi: 10.1111/j.1469-185X.2010.00148.x

Kiørboe, T. (2013). Zooplankton body composition. *Limnology and Oceanography*, *58*(5), 1843–1850. doi: 10.4319/lo.2013.58.5.1843

Kiørboe, T., & Hansen, J. L. S. (1993). Phytoplankton aggregate formation: Observations of patterns and mechanisms of cell sticking and the significance of exopolymeric material. *Journal of Plankton Research*, *15*(9), 993–1018. doi: 10.1093/plankt/15.9.993

Kulk, G., Platt, T., Dingle, J., Jackson, T., Jönsson, B. F., Bouman, H., … Raman, S. (2020). Primary production, an index of climate change in the ocean: Satellite-based estimates over two decades. *Remote Sensing*, *12*(826). doi: 10.3390/rs12050826

Kulk, G., Platt, T., Dingle, J., Jackson, T., Jönsson, B. F., Bouman, H., … Sathyendranath, S. (2021). *BICEP/NCEO: Monthly global Marine Phytoplankton Primary Production, between 1998-2020 at 9 km resolution (derived from the Ocean Colour Climate Change Initiative v4.2 dataset) [dataset].* NERC EDS Centre for Environmental Data Analysis. doi: 10.5285/69b2c9c6c4714517ba10dab3515e4ee6

Kwong, L. E., & Pakhomov, E. A. (2021). Zooplankton size spectra and production assessed by two different nets in the subarctic Northeast Pacific. *Journal of Plankton*

Research, *43*(4), 527–545. doi: 10.1093/plankt/fbab039

Lamborg, C. H., Buesseler, K. O., Valdes, J., Bertrand, C. H., Bidigare, R. R., Manganini, S. J., … Wilson, S. (2008). The flux of bio- and lithogenic material associated with sinking particles in the mesopelagic "twilight zone" of the northwest and North Central Pacific Ocean. *Deep-Sea Research Part II*, *55*(14-15), 1540–1563. doi: 10.1016/j.dsr2.2008.04.011

Lampitt, R. S., Briggs, N., Cael, B. B., Espinola, B., Hélaouet, P., Henson, S. A., … Smeed, D. (2023). Deep ocean particle ux in the Northeast Atlantic over the past 30years: carbon sequestration is controlled by ecosystem structure in the upper ocean. *Frontiers in Earth Science*, *11*. doi: 10.3389/feart.2023.1176196

Laurenceau-Cornec, E. C., Le Moigne, F. A., Gallinari, M., Moriceau, B., Toullec, J., Iversen, M. H., … De La Rocha, C. L. (2019). New guidelines for the application of Stokes' models to the sinking velocity of marine aggregates. *Limnology and Oceanography*, *65*(6), 1264–1285. doi: 10.1002/lno.11388

Laws, E. A., Falkowski, P. G., Smith, W. O., Ducklow, H. W., & McCarthy, J. J. (2000). Temperature effects on export production in the open ocean. *Global Biogeochemical Cycles*, *14*(4), 1231–1246. doi: 10.1029/1999GB001229

Le Borgne, R., & Gesbert., H. (1995). *Campagne océanographique FLUPAC à bord du N. O. l'ATALANTE (23 septembre au 29 octobre 1994). Recueil des données. Tome 2: Optique marine, matière organique dissoute, pigments photosynthétiques, observations microscopiques, production primaire, broutage,* (Tech. Rep.). Archives Sci. Mer Océanogr.

Le Moigne, F. A., Villa-Alfageme, M., Sanders, R. J., Marsay, C. M., Henson, S. A., &

García-Tenorio, R. (2013). Export of organic carbon and biominerals derived from 234Th and 210Po at the Porcupine Abyssal Plain. *Deep-Sea Research I*, *72*, 88–101. doi: 10.1016/j.dsr.2012.10.010

Lewis, E., & Wallace, D. W. R. (1998). *Program developed for CO2 system calculations* (ORNL/CDIAC ed.). Carbon Dioxide Information Analysis Center, Oak Ridge National Laboratory, US Department of Energy, Oak Ridge, TN. Retrieved from `http://cdiac.ornl.gov/oceans/co2rprt.html`

Li, X., & Logan, B. E. (1995). Size distributions and fractal properties of particles during a simulated phytoplankton bloom in a mesocosm. *Deep-Sea Research II*, *42*(1), 125–138. doi: 10.1016/0967-0645(95)00008-E

Li, Z., & Cassar, N. (2016). Satellite estimates of net community production based on O2/Ar observations and comparison to other estimates. *Global Biogeochemical Cycles*, *30*(5), 735–752. doi: 10.1002/2015GB005314

Logan, B. E., & Wilkinson, D. B. (1990). Fractal geometry of marine snow and other biological aggregates. *Limnology and Oceanography*, *35*(1), 130–136. doi: 10.4319/lo.1990.35.1.0130

Long, J. S., Fassbender, A. J., & Estapa, M. L. (2021). Depth-Resolved Net Primary Production in the Northeast Pacific Ocean: A Comparison of Satellite and Profiling Float Estimates in the Context of Two Marine Heatwaves. *Geophysical Research Letters*, *48*(19), 1–11. doi: 10.1029/2021GL093462

Maggi, F. (2013). The settling velocity of mineral, biomineral, and biological particles and aggregates in water. *Journal of Geophysical Research: Oceans*, *118*(4), 2118–2132. doi: 10.1002/jgrc.20086

Marsay, C. M., Sanders, R. J., Henson, S. A., Pabortsava, K., & Achterberg, E. P. (2015). Attenuation of sinking particulate organic carbon flux through the mesopelagic ocean. *Proceedings of the National Academy of Sciences*, *112*(4), 1089–1094. doi: 10.1073/pnas.1415311112

Martin, J. H., Knauer, G. A., Karl, D. M., & Broenkow, W. W. (1987). VERTEX: Carbon cycling in the northeast Pacific. *Deep-Sea Research*, *34*(2), 267–285. doi: 10.1016/0198-0149(87)90086-0

McDougall, T. J., & Barker, P. M. (2011). *Getting started with TEOS-10 and the Gibbs Seawater (GSW) oceanographic Toolbox*. SCOR/IAPSO WG127.

McKinna, L., Cetinić, I., Chase, A., & Werdell, P. (2019). Approach for Propagating Radiometric Data Uncertainties Through NASA Ocean Color Algorithms. *Frontiers in Earth Science*, *7*. doi: 10.3389/feart.2019.00176

Meng, S., & Liu, Y. (2016). New insights into transparent exopolymer particles (TEP) formation from precursor materials at various Na+/Ca2+ ratios. *Scientific Reports*, *6*, 19747. doi: 10.1038/srep19747

Miklasz, K. A., & Denny, M. W. (2010). Diatom sinking speeds: Improved predictions and insight from a modified Stokes' law. *Limnology and Oceanography*, *55*(6), 2513–2525. doi: 10.4319/lo.2010.55.6.2513

Miller, C. B., Frost, B. W., Wheeler, P. A., Landry, M. R., Welschmeyer, N., & Powell, T. M. (1991). Ecological dynamics in the subarctic Pacific, a possibly iron-limited ecosystem. *Limnology and Oceanography*, *36*(8), 1600–1615. doi: 10.4319/lo.1991.36.8.1600

Morel, A. (1988). Optical modeling of the upper ocean in relation to its biogenous matter content. *Journal of Geophysical Research*, *93*, 1074910768. doi: 10.1029/JC093iC09p10749

Morel, A., Huot, Y., Gentili, B., Werdell, P. J., Hooker, S. B., & Franz, B. A. (2007). Examining the consistency of products derived from various ocean color sensors in open ocean (Case 1) waters in the perspective of a multi-sensor approach. *Remote Sensing of Environment*, *111*(1), 69–88. doi: 10.1016/j.rse.2007.03.012

Moriarty, R., & O'Brien, T. D. (2013). Distribution of mesozooplankton biomass in the global ocean. *Earth System Science Data*, *5*(1), 45–55. doi: 10.5194/essd-5-45-2013

Murray, J. W., Young, J., Newton, J. A. N., Dunne, J. P., Chapin, T., Paul, B., & Mccarthys, J. J. (1996). Export flux of particulate organic carbon from the central equatorial Pacific determined using a combined drifting trap-234Th approach. *Deep-Sea Research II*, *43*(4-6), 1095–1132. doi: 10.1016/0967-0645(96)00036-7

Nayar, K. G., Sharqawy, M. H., Banchik, L. D., & Lienhard, J. H. (2016). Thermophysical properties of seawater: A review and new correlations that include pressure dependence. *Desalination*, *387*, 1–24. doi: 10.1016/j.desal.2016.02.024

Nöthig, E.-M., Bracher, A., Engel, A., Metfies, K., Niehoff, B., Peeken, I., ... Wurst, M. (2015). Summertime plankton ecology in Fram Strait –a compilation of long- and short-term observations. *Polar Research*, *34*. doi: 10.3402/polar.v34.23349

Olsen, A., Key, R. M., van Heuven, S., Lauvset, S. K., Velo, A., Lin, X., ... Suzuki, T. (2016). The Global Ocean Data Analysis Project version 2 (GLODAPv2) -an internally consistent data product for the world ocean. *Earth System Science Data*, *8*, 297–323. doi: 10.5194/essd-8-297-2016

Passow, U. (2002). Transparent exopolymer particles (TEP) in aquatic environments.

Progress in Oceanography, *55*(3–4), 287–333. doi: 10.1016/S0079-6611(02)00138-6

Pearson, B., & Fox-Kemper, B. (2018). Log-Normal turbulence dissipation in global ocean models. *Physical Review Letters*, *120*(094501). doi: 10.1103/PhysRevLett.120.094501

Petrik, C. M., Luo, J. Y., Heneghan, R. F., Everett, J. D., Harrison, C. S., & Richardson, A. J. (2022). Assessment and constraint of mesozooplankton in CMIP6 Earth System Models. *Global Biogeochemical Cycles*, *36*(11). doi: 10.1029/2022GB007367

Reagan, J. R., Boyer, T. P., García, H. E., Locarnini, R. A., Baranova, O. K., Bouchard, C., … Dukhovskoy, D. (2024). *World Ocean Atlas 2023. NOAA National Centers for Environmental Information. (NCEI Accession 0270533) [dataset].* Retrieved from `https://www.ncei.noaa.gov/access/world-ocean-atlas-2023/`

Roca-Martí, M., Benitez-Nelson, C. R., Umhau, B. P., Wyatt, A. M., Clevenger, S. J., Pike, S., … Buesseler, K. O. (2021). Concentrations, ratios, and sinking fluxes of major bioelements at Ocean Station Papa. *Elementa: Science of the Anthropocene*, *9*(1), 00166. doi: 10.1525/elementa.2020.00166

Rufas, A. (2021). *Dataset on the cellular quota, volume and diameter of four major groups of marine phytoplankton [dataset].* Zenodo.

Rufas, A., Khatiwala, S., Bisson, K. M., Martin, A. P., & Bouman, H. A. (2025). Can we constrain geographical variability in the biological carbon pump's transfer efficiency from observations? *Geophysical Research Letters*, *52*, e2024GL111203. doi: 10.1029/2024GL111203

Saiz, E., & Kiørboe, T. (1995). Predatory and suspension feeding of the copepod Acartia tonsa in turbulent environments. *Marine Ecology Progress Series*, *122*, 147–158. doi:

10.3354/meps122147

Sathyendranath, S., Jackson, T., Brockmann, C., Brotas, V., Calton, B., Chuprin, A., . . . Regner, T. (2020). *ESA Ocean Colour Climate Change Initiative (Ocean_Colour_cci): Global chlorophyll-a data products gridded on a geographic projection, Version 4.2 [dataset].* Centre for Environmental Data Analysis. Retrieved from `https://catalogue.ceda.ac.uk/uuid/5400de38636d43de9808bfc0b500e863/`

Sathyendranath, S., Jackson, T., Brockmann, C., Brotas, V., Calton, B., Chuprin, A., . . . Vale, T. (2023). *ESA Ocean Colour Climate Change Initiative (Ocean_Colour_cci): Monthly climatology of global ocean colour data products at 4km resolution, Version 6.0 [dataset].* NERC EDS Centre for Environmental Data Analysis. Retrieved from `https://catalogue.ceda.ac.uk/uuid/690fdf8f229c4d04a2aa68de67beb733/`

Schulz, M., Prospero, J. M., Baker, A. R., Dentener, F., Ickes, L., Liss, P. S., . . . Duce, R. A. (2012). Atmospheric transport and deposition of mineral dust to the ocean: Implications for research needs. *Environmental Science and Technology*, *46*(19), 10390–10404. doi: 10.1021/es300073u

Sharqawy, M. H., Lienhard, J. H., & Zubair, S. M. (2010). Thermophysical properties of seawater: A review of existing correlations and data. *Desalination and Water Treatment*, *16*(1-3), 354–380. doi: 10.5004/dwt.2010.1

Shima, S. I., Kusano, K., Kawano, A., Sugiyama, T., & Kawahara, S. (2009). The super-droplet method for the numerical simulation of clouds and precipitation: A particle-based and probabilistic microphysics model coupled with a non-hydrostatic model. *Quarterly Journal of the Royal Meteorological Society*, *135*(642), 1307–1320. doi: 10.1002/qj.441

Sieburth, J. M. N., Smetacek, V., & Lenz, J. (1978). Pelagic ecosystem structure: Heterotrophic compartments of the plankton and their relationship to plankton size fractions. *Limnology and Oceanography*, *23*(6), 1256–1263. doi: 10.4319/lo.1978.23.6.1256

Silsbe, G. M., Behrenfeld, M. J., Halsey, K. H., Milligan, A. J., & Westberry, T. (2016). The CAFE model: A net production model for global ocean phytoplankton. *Global Biogeochemical Cycles*, *30*(12), 1756–1777. doi: 10.1002/2016GB005521

Stamieszkin, K., Pershing, A. J., Record, N. R., Pilskaln, C. H., Dam, H. G., & Feinberg, L. R. (2015). Size as the master trait in modeled copepod fecal pellet carbon flux. *Limnology and Oceanography*, *60*(6), 2090–2107. doi: 10.1002/lno.10156

Stokes, G. G. (1851). On the effect of the internal friction of fluids on the motion of pendulums. In *Transactions of the cambridge philosophical society* (Vol. 9, pp. 8–106).

Timmerman, A. H. V., & Hamme, R. C. (2021). Consistent Relationships Among Productivity Rate Methods in the NE Subarctic Pacific. *Global biogeochemical Cycles*, *35*(2). doi: 10.1029/2020GB006721

Timothy, D. A., Wong, C. S., Page, J., White, L. A., & Macdonald, R. W. (2013). Climatology of sediment flux and composition in the subarctic Northeast Pacific Ocean with biogeochemical implications. *Progress in Oceanography*, *116*, 95–129. doi: 10.1016/j.pocean.2013.06.017

UK Met Office. (2005). *GHRSST Level 4 OSTIA Global Foundation Sea Surface Temperature Analysis, version 1.0 [dataset].* Physical Oceanography Distributed Active Archive Center. Retrieved from `https://podaac.jpl.nasa.gov/dataset/`

`UKMO-L4HRfnd-GLOB-OSTIA` doi: 10.5067/GHOST-4FK01

Van Heuven, S., Pierrot, D., Rae, J. W. B., Lewis, E., & Wallace, D. W. R. (2011). *MATLAB program developed for CO2 system calculations* (Vol. ORNL/CDIAC). Carbon Dioxide Information Analysis Center, Oak Ridge National Laboratory, U.S. Department of Energy, Oak Ridge, Tennessee. doi: 10.3334/CDIAC/otg.CO2SYSS_MATLAB_v1.1

Welschmeyer, N. A., Strom, S., Goericke, R., DiTullio, G., Belvin, M., & Petersen, W. (1993). Primary production in the subarctic Pacific Ocean: Project SUPER. *Progress in Oceanography*, *32*, 101–135. doi: 10.1016/0079-6611(93)90010-B

Westberry, T., Behrenfeld, M. J., Siegel, D. A., & Boss, E. S. (2008). Carbon-based primary productivity modeling with vertically resolved photoacclimation. *Global Biogeochemical Cycles*, *22*(2), GB2024. doi: 10.1029/2007GB003078

White, F. M. (1974). *Viscous fluid flow.* New York: McGraw Hill.

Wong, C. S., Waser, N. A. D., Whitney, F. A., Johnson, W. K., & Page, J. (2002). Time-series study of the biogeochemistry of the North East subarctic Pacific: Reconciliation of the Corg/N remineralization and uptake ratios with the Redfield ratios. *Deep-Sea Research II*, *49*(24-25), 5717–5738. doi: 10.1016/S0967-0645(02)00211-4

Wong, C. S., Whitney, F. A., Iseki, K., Page, J. S., & Zeng, J. (1995). Analysis of trends in primary productivity and chlorophyll-a over two decades at Ocean Station P (50°N, 145°W) in the subarctic northeast Pacific Ocean. In R. J. Beamish (Ed.), *Climate change and northern fish populations* (pp. 107–117). Ottawa: Canadian Special Publication of Fisheries and Aquatic Sciences, 121.

Table S1. Pearson correlation coefficient (r^2) between monthly means of depth-integrated NPP from five satellite-based NPP models (VGPM, CbPM, CAFE, BICEP, and Carr (2002)) and their *in situ* ^{14}C-based observations counterparts at stations ALOHA ($N = 12$), BATS ($N = 12$), EqPac ($N = 5$), and OSP ($N = 10$) (all data are plotted in Figure S5). For each location, the best-performing model statistics are highlighted in green, and the second-best in yellow.

	ALOHA	BATS	EqPac	OSP
VGPM (MODIS)	0.28	0.51	0.50	0.44
CbPM (MODIS)	0.31	0.07	0.00	0.49
CAFE (MODIS)	0.88	0.67	0.02	0.46
BICEP (merged sensors)	0.66	0.81	0.14	0.49
Carr 2002 (MODIS, C02)	0.07	0.79	0.00	0.60

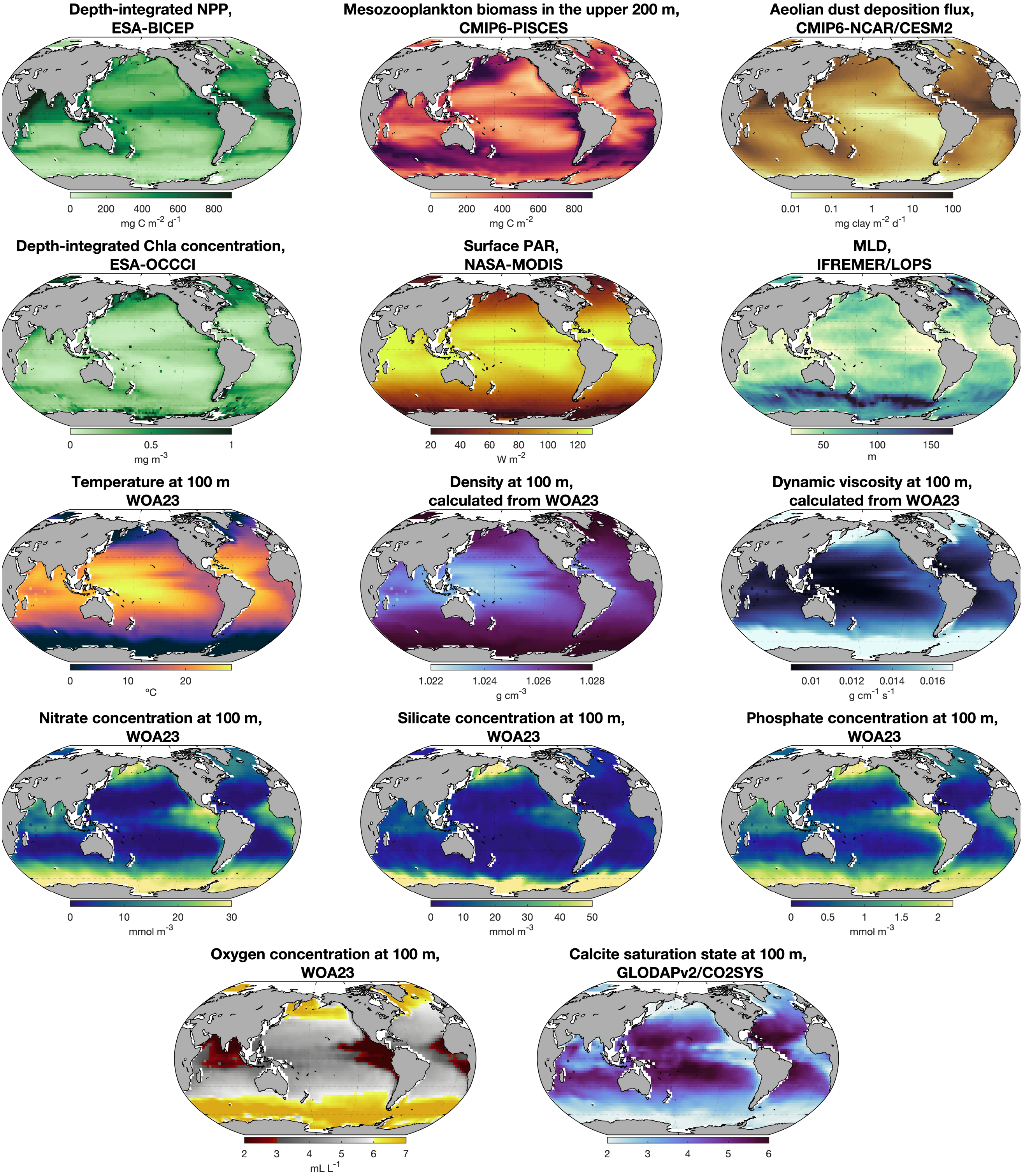

Figure S1. Global ocean distribution of the climatological annual mean of the variables used to force SLAMS-2.0.

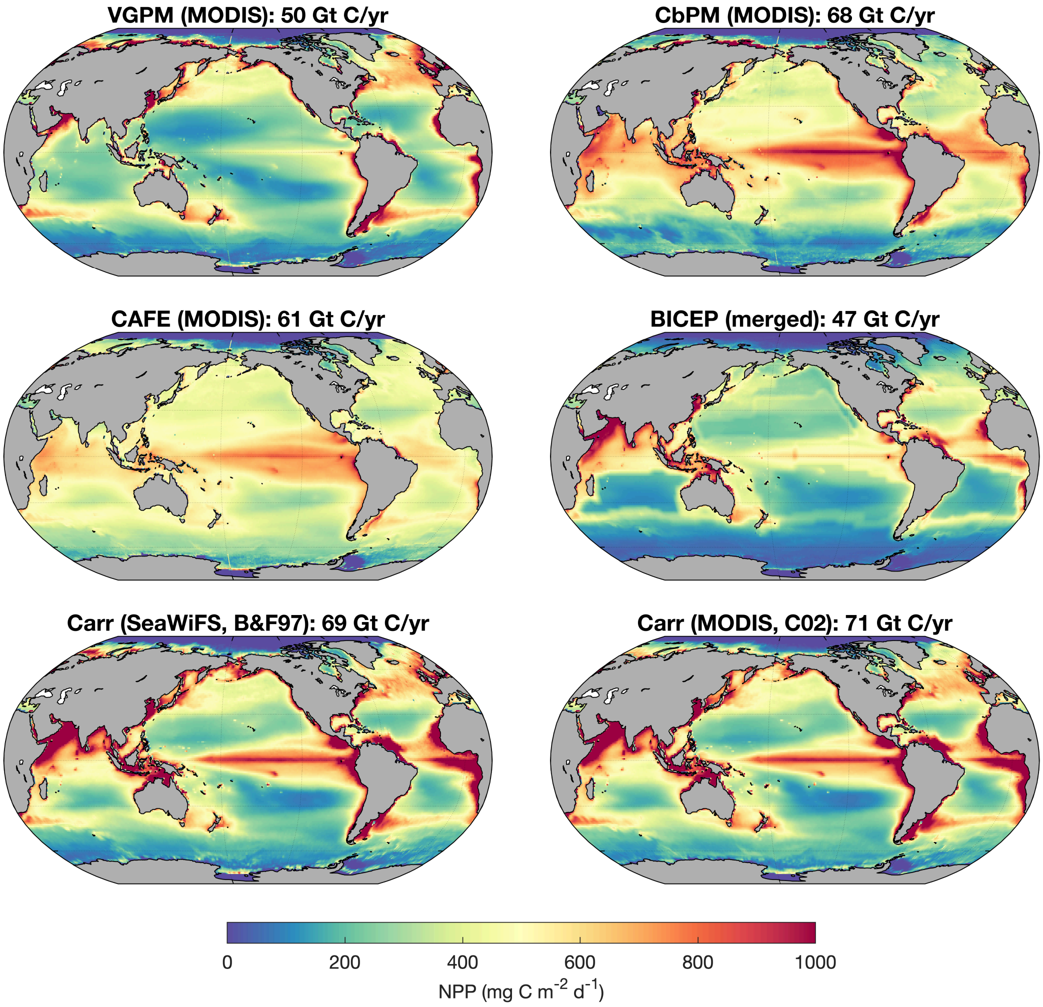

Figure S2. Global distribution of depth-integrated annual net primary production (NPP) from five ocean-colour-based models: (A) VGPM (Vertically Generalized Productivity Model, Behrenfeld & Falkowski, 1997); (B) CbPMv2 (Carbon-based Production Model-2, Westberry et al., 2008); (C) CAFE (Carbon, Absorption, and Fluorescence Euphotic-resolving model, Silsbe et al., 2016); (D) BICEP (Biological Pump and Carbon Exchange Processes project model, Kulk et al., 2020); (E–F) NPP model of Carr (2002), shown in two configurations. VGPM, CbPMv2, and CAFE use MODIS-Aqua inputs (Chl*a*, PAR$_0$, SST) and are available as finished products at the Ocean Productivity site (`http://sites.science.oregonstate.edu/ocean.productivity/`). The BICEP product is a merged multi-sensor product and is accessible via the ESA Ocean Colour Climate Change Initiative website (`http://www.oceancolour.org`). The Carr model was run using (E) SeaWiFS Chl*a* and PAR$_0$ with the euphotic depth formulation of Behrenfeld and Falkowski (1997) (as applied by Henson et al. (2012)), and (F) MODIS-Aqua Chl*a* and PAR$_0$ with the original euphotic depth of Carr (2002); both configurations use AVHRR Pathfinder v5.0 SST (1985–2001) (`https://www.ncei.noaa.gov/products/avhrr-pathfinder-sst`). MODIS-Aqua and SeaWiFS data were obtained from NASA Ocean Color website (`https://oceandata.sci.gsfc.nasa.gov/l3/`).

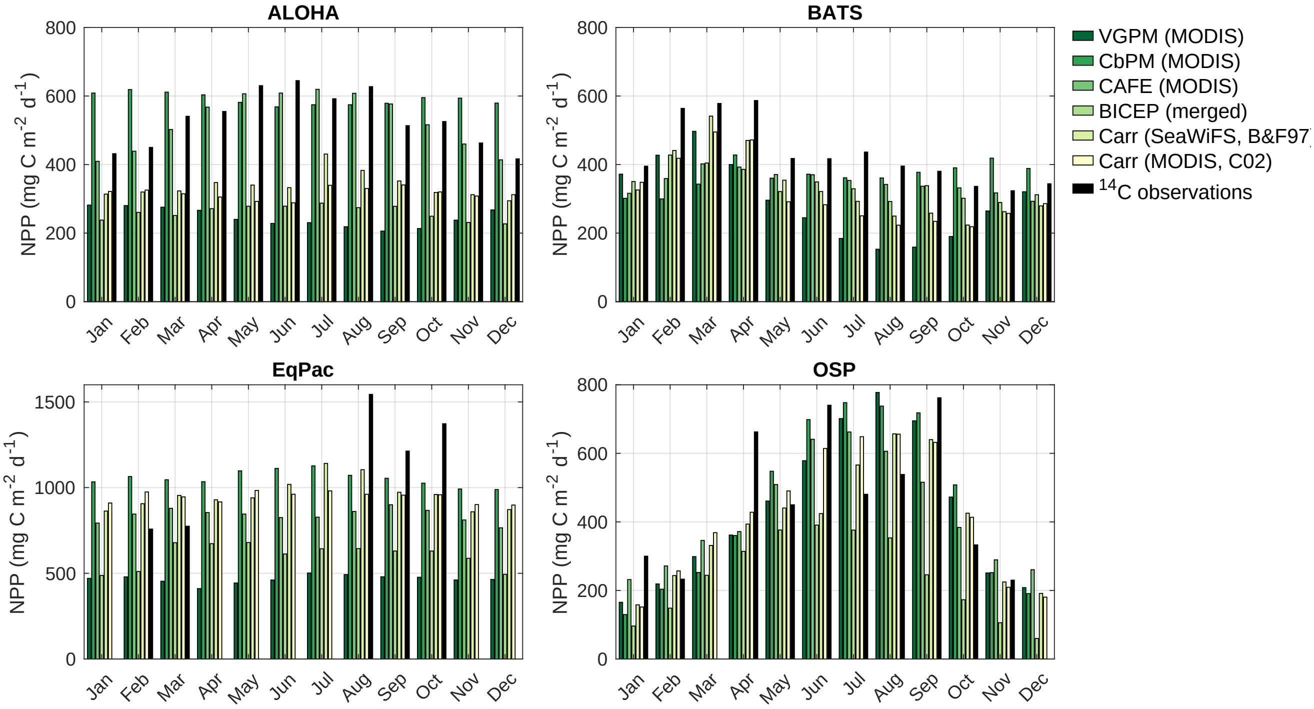

Figure S3. Comparison of monthly mean depth-integrated NPP at four ocean sites (ALOHA, BATS, EqPac, and OSP). Data include satellite-derived estimates from five ocean-colour-based models (VGPM, CbPM, CAFE, BICEP, and Carr (2002); see Figure S2) and *in situ* ^{14}C uptake measurements. ^{14}C data sources are: ALOHA (1989–2018, Karl et al., 2021, Supplementary Table 1); BATS (1988–2022, Bates et al., 2023); EqPac (Murray et al. (1996), Table 5, 2°N–2°S; Le Borgne and Gesbert. (1995), Ch. 11, stations 94 and 100); and OSP (compiled from Long et al. (2021) and sources therein —Booth (1988), Miller et al. (1991), Welschmeyer et al. (1993), Wong et al. (1995), Boyd and Harrison (1999), Kawakami et al. (2010), Giesbrecht et al. (2012), Timmerman and Hamme (2021)— as well as in the synthesis study for the OSP time-series site (1987–1996, Timothy et al., 2013, Fig. 2(i)).

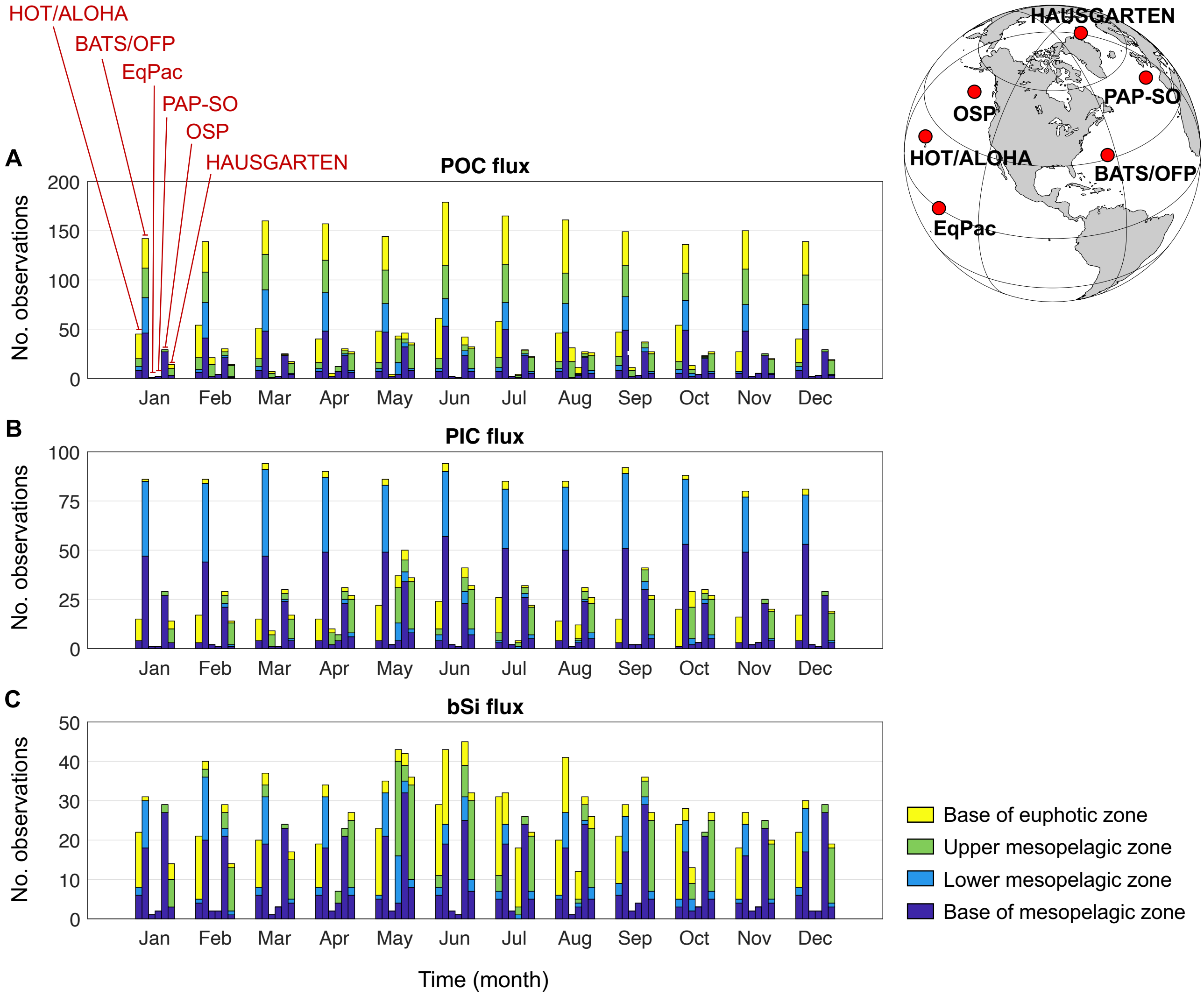

Figure S4. Number of (A) POC, (B) PIC, and (C) bSi flux observations from sediment traps and radionuclide disequilibrium contributing to the monthly-averaged depth values shown in Figure S5. Data are grouped by month for each of our six study sites (HOT/ALOHA, BATS/OFP, EqPac, PAP-SO, OSP, HAUSGARTEN) and by depth zone (base of the euphotic zone, upper, lower, and base mesopelagic; see Table S2). In total, $N = 7162$ POC, $N = 5282$ PIC, and $N = 3856$ bSi flux measurements were compiled, of which $N = 3240$, $N = 2079$, and $N = 1451$ were used for model optimisation after depth selection. The inset map shows the geographical locations of the six sites: HOT/ALOHA (subtropical NE Pacific), BATS/OFP (subtropical NW Atlantic), EqPac (central equatorial Pacific), PAP-SO (subpolar NE Atlantic), OSP (subpolar NE Pacific), and HAUSGARTEN (subarctic Atlantic).

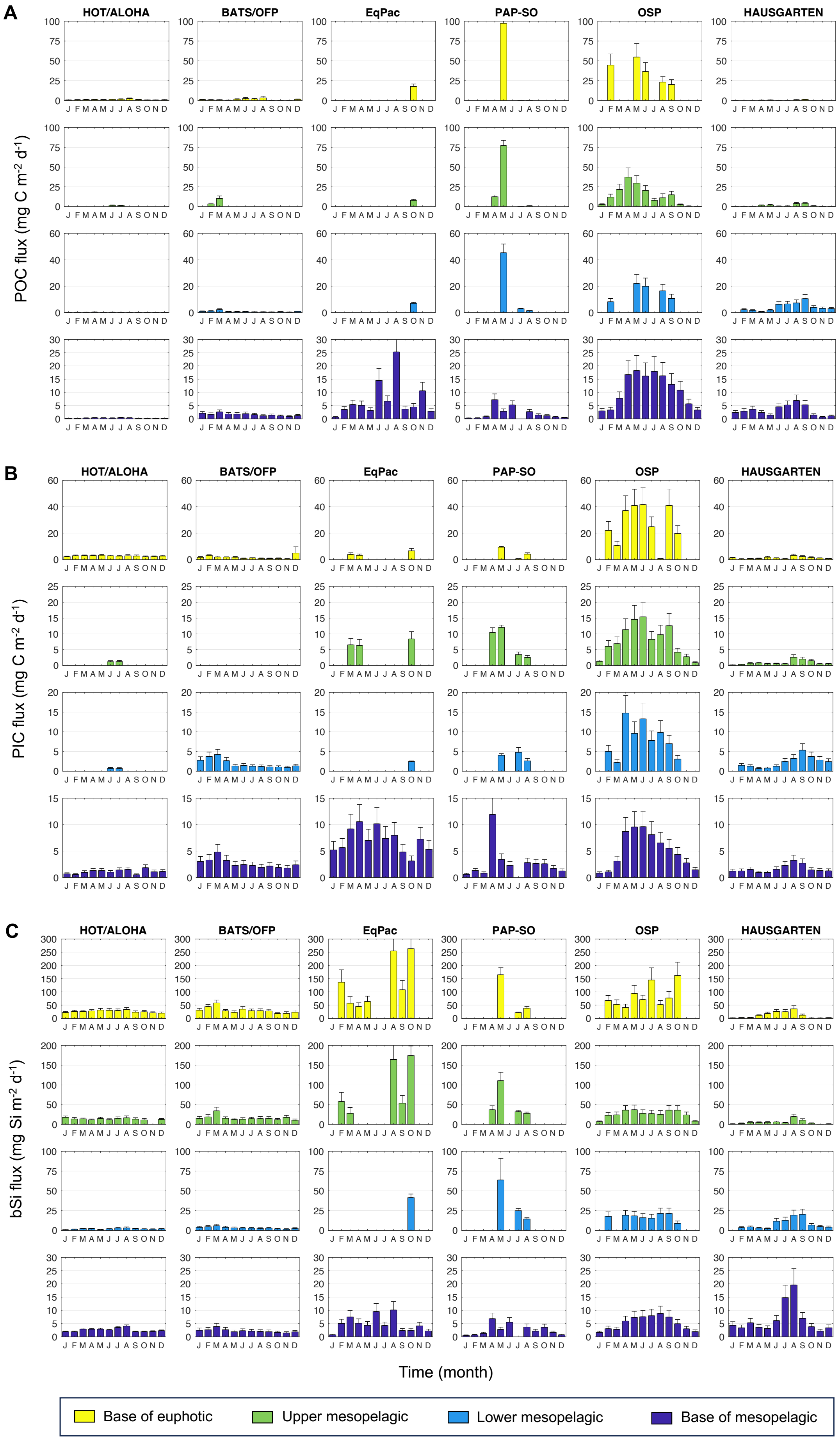

Figure S5. Observed monthly mean fluxes of (A) POC, (B) PIC, and (C) bSi compiled from sediment traps and radionuclides at our six ocean study sites. Vertical error bars indicate net uncertainty and has been calculated as the quadratic sum of systematic and random errors propagated from measured values.

Figure S6. Observed monthly mean flux ratios of two ballast minerals relative to POC across our six ocean study sites. (A) Calcium carbonate (PIC, mainly from coccolithophore carbonated shells) to POC. (B) Biogenic silica (Si, mainly from diatom frustules) to POC. Ratios are derived from sediment trap and radionuclide data shown in Figure S7.

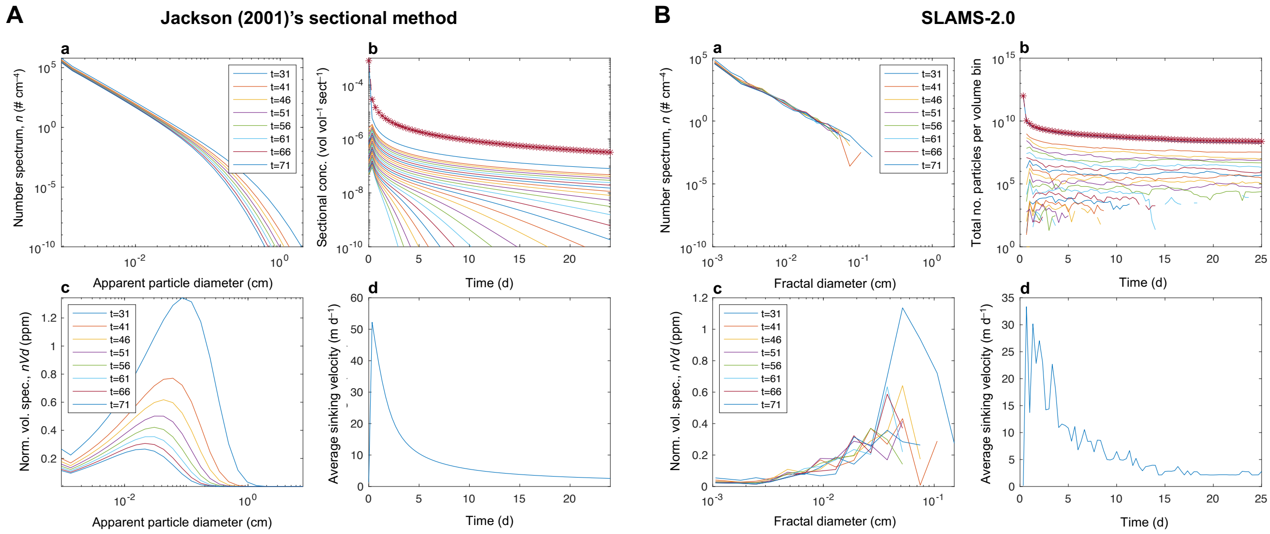

Figure S7. Comparison of two particle coagulation approaches. (A) Solution of the Smoluchowski equation using a sectional population-balance approach with fractal kernels following Jackson (2001) (implementation from Jackson, 2004). (B) SLAMS-2.0's coagulation subroutine based on the Super-Droplet Method (SDM; Shima et al., 2009), which visually converges to the Smoluchowski solution. Both simulations are initialised with a particle concentration of 10^6 particles cm^{-3} in the smallest size class and run for 25 modelled days (with a 1/3-day time step) in a 50 m deep mixed layer. In SLAMS-2.0, particles are represented by 1000 superparticles with fractal dimension 2. Panels (a) and (b) show the evolution of the particle number spectrum and total mass concentration across 27 size classes, respectively. Both simulations exhibit rapid transfer of particles toward larger sizes via coagulation, with SLAMS-2.0 converging to the Smoluchowski solution as coagulation and settling losses balance. For smaller particles, coagulation losses exceed settling, while for larger particles, settling losses become larger than coagulation losses.

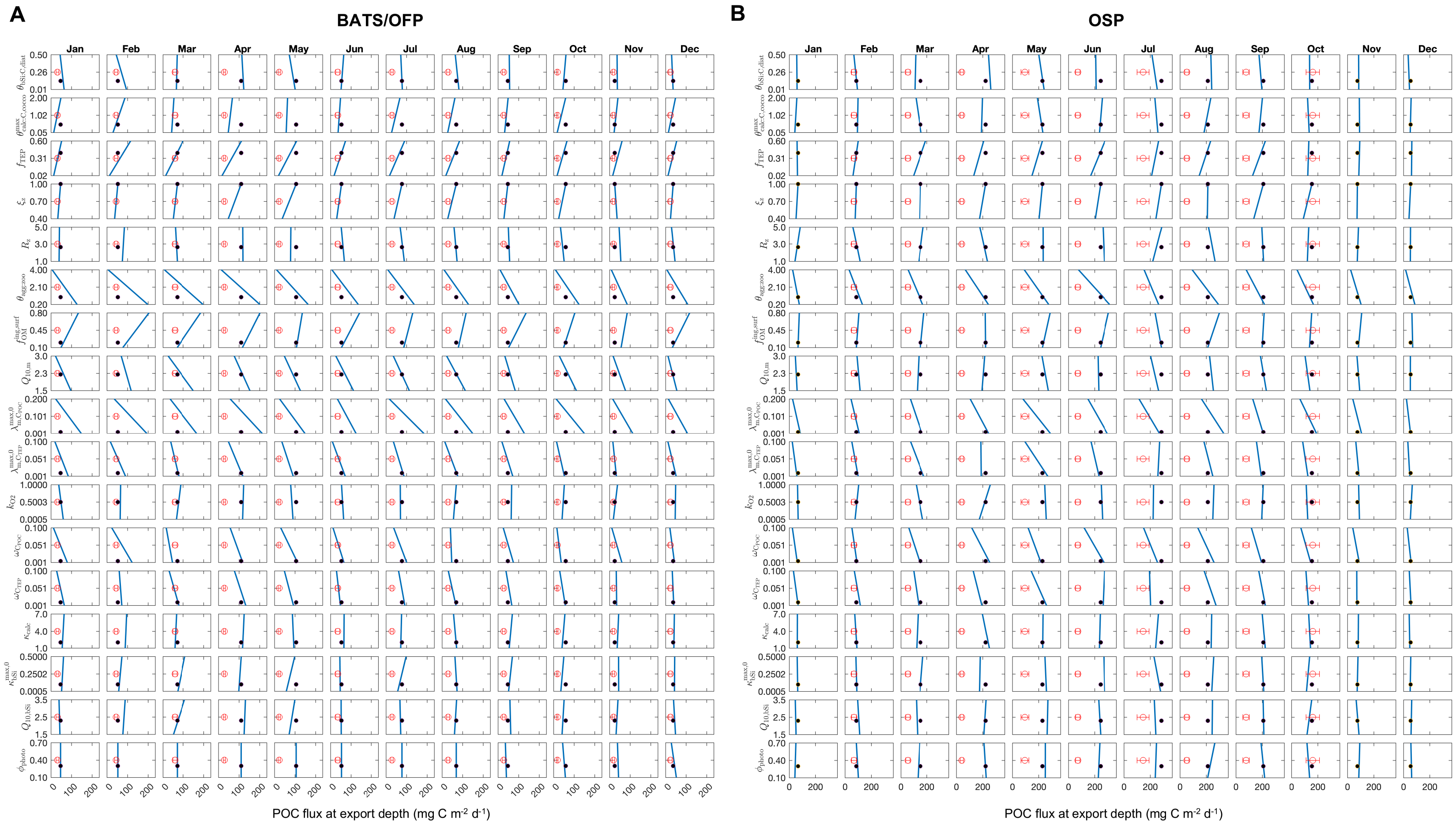

Figure S8. Parameter sensitivity of simulated particulate organic carbon (POC) flux at the export depth for two study sites (A and B). Rows correspond to the 17 tested parameters and columns to months of the year. Blue lines connect model outputs obtained using the minimum and maximum literature-supported parameter values; black dots indicate default model output, and red dots indicate observations.

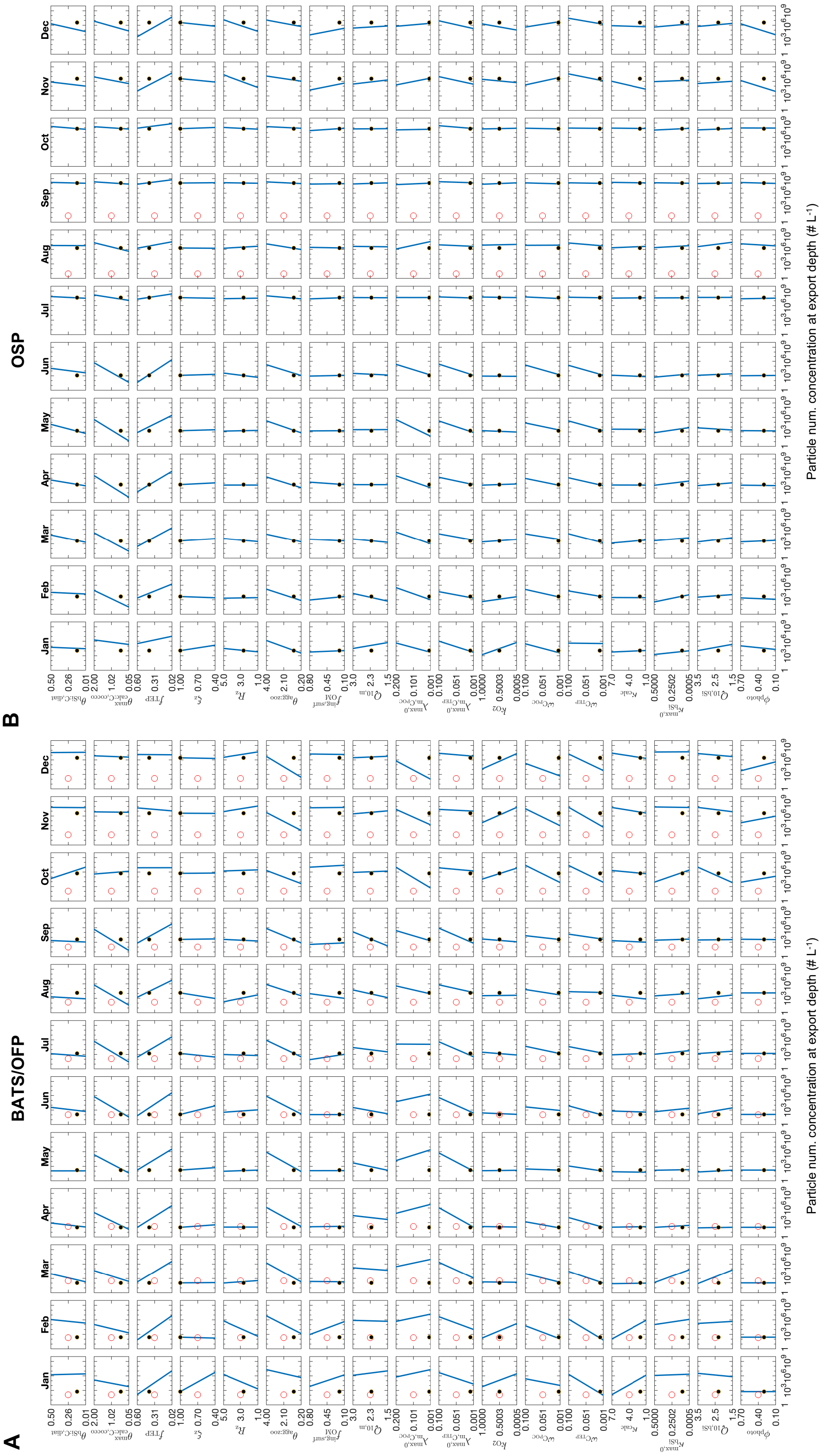

Figure S9. As in Figure S8, but for particle number concentration at the export depth.

Table S2. Depth zone ranges (in metres) used to extract both observed and modelled fluxes of POC, PIC, and bSi at our six study sites: HOT/ALOHA, BATS/OFP, EqPac, PAP-SO, OSP, and HAUSGARTEN. For the "Base of euphotic" category, monthly depth ranges are shown, and blank cells indicate months with no available observational data. For the mesopelagic layers, depth ranges are shown as fixed values across all months, even though observational data were not always available in every month.

	HOT/ALOHA				BATS/OFP				EqPac			
	z_{eu}	POC	PIC	bSi	z_{eu}	POC	PIC	bSi	z_{eu}	POC	PIC	bSi
Base of euphotic	115–142	135–165	135–165	135–165	96–118	135–165	135–165	135–165	83–103	–	–	–
	119–147	135–165	135–165	135–165	92–114	135–165	135–165	135–165	83–102	90–110	–	–
	95–117	135–165	135–165	135–165	93–115	135–165	135–165	135–165	68–84	67–83	72–88	–
	97–120	135–165	135–165	135–165	85–105	135–165	135–165	135–165	68–84	90–110	72–88	–
	101–125	135–165	135–165	135–165	105–130	135–165	135–165	135–165	80–98	90–110	–	–
	102–126	135–165	135–165	135–165	111–137	135–165	135–165	135–165	77–95	–	–	–
	98–121	135–165	135–165	135–165	115–142	135–165	135–165	135–165	75–93	–	–	–
	97–120	135–165	135–165	135–165	117–144	135–165	135–165	135–165	77–95	75–100	–	–
	125–154	135–165	135–165	135–165	110–136	135–165	135–165	135–165	81–100	90–110	–	–
	120–148	135–165	135–165	135–165	136–167	135–165	135–165	135–165	81–100	94–116	90–110	94–116
	115–141	135–165	135–165	135–165	116–143	135–165	135–165	135–165	83–103	–	–	–
	110–136	135–165	135–165	135–165	101–125	135–165	135–165	135–165	83–103	–	–	–
Upper mesopelagic		290–310	290–310	290–310		290–310	290–310	290–310		150–200	150–200	150–200
Lower mesopelagic		790–810	490–510	790–810		490–510	490–510	490–510		310–330	310–330	310–330
Base of mesopelagic		1490–1510	1490–1510	1490–1510		1490–1510	1490–1510	1490–1510		870–890	870–890	870–890

	PAP-SO				OSP				HAUSGARTEN			
	z_{eu}	POC	PIC	bSi	z_{eu}	POC	PIC	bSi	z_{eu}	POC	PIC	bSi
Base of euphotic	82–101	–	–	–	71–88	–	–	–	60–75	161–197	161–197	161–197
	82–101	–	–	–	73–90	90–110	90–110	90–110	63–78	72–88	72–88	72–88
	77–95	–	–	–	72–89	90–110	90–110	–	65–81	72–88	72–88	72–88
	61–76		–	–	73–90	90–110	90–110	–	68–84	72–88	72–88	72–88
	57–71	54–66	67–83	54–66	71–88	90–110	90–110	90–110	37–46	72–88	72–88	72–88
	53–66	–	–	–	69–85	90–110	90–110	90–110	35–43	72–88	72–88	72–88
	56–70	61–75	61–75	48–64	61–75	45–55	45–55	–	44–55	72–88	72–88	72–88
	60–75	50–68	50–68	50–68	65–81	65–80	65–80	65–80	55–68	72–88	72–88	72–88
	63–78	–	–	–	64–79	45–55	45–55	45–55	50–62	72–88	72–88	72–88
	62–77	–	–	–	63–78	45–55	45–55	–	53–65	72–88	72–88	72–88
	68–84	–	–	–	62–77	–	–	–	55–69	72–88	72–88	72–88
	77–95	–	–	–	64–79	–	–	–	58–72	72–88	72–88	72–88
Upper mesopelagic		171–200	171–200	171–200		250–300	250–300	250–300		270–320	270–320	270–320
Lower mesopelagic		446–500	446–500	446–500		590–610	590–610	590–610		790–810	790–810	790–810
Base of mesopelagic		990–1010	990–1010	990–1010		990–1010	990–1010	990–1010		1220–1260	1220–1260	1220–1260

Table S3. Comparison of modelled and observed particle attributes of six primary particle types seeded in SLAMS-2.0: diatoms, coccolithophores, large flagellated phytoplankton, picophytoplankton, transparent exopolymer particles (TEPs), and aeolian-borne clays. Observational data are compiled from 32 references in Rufas (2021). Where observed diameters were unavailable, they were estimated from volume assuming spherical shape. Modelled sinking velocities were calculated using a global mean seawater density ($1.0262\ \mathrm{g\,cm^{-3}}$) and dynamic viscosity ($0.0134\ \mathrm{g\,cm^{-1}\,s^{-1}}$) for the upper 200 m, based on World Ocean Atlas 2023 data.

Primary particle	Density ($\mathrm{g\,cm^{-3}}$)	Volume ($\mu\mathrm{m}^3$)		Diameter (μm)		Sinking velocity ($\mathrm{m\,d^{-1}}$)	
		Model	Obs.	Model	Obs.	Model	Obs.
Diatom	1.21	$256 - 127,940$	$100 - 10^7$	$7.9 - 63$	$4.0 - 200$	$0.40 - 25$	$0.30 - 35$[c]
Cocco.	1.84	$32 - 197$	$25 - 10^4$	$3.9 - 7.2$	$3.0 - 14$	$0.44 - 1.5$	$0.15 - 10$[d]
Flagel.	1.06	$8,393 - 209,840$	$200 - 10^7$	$25 - 74$	$10 - 200$	$0.76 - 6.5$	
Pico.	1.06	$0.042 - 2.1$	$0.10 - 25$	$0.43 - 1.6$	$0.60 - 4.0$	$0.0002 - 0.0030$	
TEP	0.80	$158 - 15,804$		$6.7 - 31$	$1 - 100$[a]	$-(0.36 - 7.7)$	
Clay	2.70	14		3.0	$0.10 - 20$[b]	0.54	

[a] (Passow, 2002). [b] (Schulz et al., 2012). [c] (Miklasz & Denny, 2010). [d] (Jansen et al., 2002).